



1 **An assessment of latest Cretaceous *Pycnodonte vesicularis* (Lamarck, 1806) shells as records for**  
2 **palaeoseasonality: A multi-proxy investigation**

3 de Winter, Niels J.\*<sup>1</sup>, Vellekoop, Johan\*<sup>1,2</sup>, Vorrsselmans, Robin<sup>2</sup>, Golreihan, Asefeh<sup>2</sup>, Soete, Jeroen<sup>2</sup>,  
4 Petersen, Sierra V.<sup>3</sup>, Meyer, Kyle W.<sup>3</sup>, Casadio, Silvio<sup>4</sup>, Speijer, Robert P.<sup>2</sup>, Claeys, Philippe<sup>1</sup>

5 <sup>1</sup>*Analytical, Environmental and Geo-Chemistry (AMGC), Vrije Universiteit Brussel (VUB), Brussels,*  
6 *Belgium.*

7 <sup>2</sup>*Department of Earth and Environmental Science, KU Leuven, Heverlee, Belgium*

8 <sup>3</sup>*Earth and Environmental Sciences Department, University of Michigan, Ann Arbor, Michigan, USA.*

9 <sup>4</sup>*Escuela de Geología, Paleontología y Enseñanza de las Ciencias, Universidad Nacional de Río Negro,*  
10 *CONICET, General Roca, Argentina.*

11

12 \*Niels J. de Winter and Johan Vellekoop contributed equally to this work

13

14 Corresponding author: [niels.de.winter@vub.be](mailto:niels.de.winter@vub.be)

15

16 Target journal: Climate of the Past

17

18 **Abstract**

19 In order to assess the potential of the honeycomb oyster *Pycnodonte vesicularis* for the  
20 reconstruction of palaeoseasonality, several specimens recovered from the late Maastrichtian  
21 Neuquén Basin (Argentina) were subject to a multi-proxy investigation, involving scanning  
22 techniques, trace element and isotopic analysis. Combined CT scanning and light microscopy reveals  
23 two major calcite micromorphologies in *P. vesicularis* shells (vesicular and foliated calcite). Micro-  
24 XRF analysis and cathodoluminescence microscopy show that reducing pore fluids were able to  
25 migrate through the vesicular portions of the shells (aided by bore holes) and cause recrystallization  
26 and precipitation of secondary carbonate in the porous micromorphology, thus rendering the  
27 vesicular portions not suitable for palaeoenvironmental reconstruction. In contrast, stable isotope  
28 and trace element compositions show that the original chemical composition of the shell is well-  
29 preserved in the denser, foliated portions, which can therefore be reliably used for the  
30 reconstruction of palaeoenvironmental conditions. Stable oxygen and clumped isotope thermometry  
31 on carbonate from the dense hinge region yield sea water temperatures of 11°C, while previous  
32 TEX<sub>86</sub><sup>H</sup> palaeothermometry yielded much higher temperatures. The difference is ascribed to seasonal  
33 bias in the growth of *P. vesicularis*, causing warm seasons to be underrepresented from the record,  
34 and TEX<sub>86</sub><sup>H</sup> palaeothermometry being potentially biased towards warmer surface water  
35 temperatures. Superimposed on this annual mean is a seasonality in δ<sup>18</sup>O of about 1‰, which is  
36 ascribed to a combination of varying salinity due to fresh water input in the winter and spring season  
37 and a moderate temperature seasonality. Attempts to independently verify the seasonality in sea  
38 water temperature by Mg/Ca ratios of shell calcite are hampered by significant uncertainty due to  
39 the lack of proper transfer functions for pycnodontin oysters. The multi-proxy approach employed  
40 here enables us to differentiate between well-preserved and diagenetically altered portions of the  
41 shells and provides an improved methodology for reconstructing palaeoenvironmental conditions in  
42 deep time. While establishing a chronology for these shells was severely complicated by growth



43 cessations and diagenesis, cyclicity in trace elements and stable isotopes allowed a tentative  
44 interpretation of the potential annual seasonal cycle in the late Maastrichtian palaeoenvironment of  
45 the Neuquén basin. Future studies of fossil ostreid bivalves should target dense foliated calcite  
46 rather than sampling bulk or vesicular calcite. Successful application of clumped isotope  
47 thermometry on fossil bivalve calcite in this study indicates that temperature seasonality in fossil  
48 ostreid bivalves may be constrained by the sequential analysis of well-preserved foliated calcite  
49 samples using this method.

50

## 51 1. Introduction

52 The Late Cretaceous is generally considered a greenhouse world (e.g. Hay, 2008). Indeed,  
53 reconstructed global mean temperatures and atmospheric pCO<sub>2</sub> concentrations for this period  
54 generally exceed those of the present-day climate (e.g., Berner, 1990; Andrews et al., 1995; Ekart et  
55 al., 1999; Hunter et al, 2008; Quan et al., 2009; Wang et al., 2013). As such, the Late Cretaceous may  
56 be considered an analogue for climate in the near future if anthropogenic greenhouse gas emissions  
57 continue unabated (IPCC, 2014; Hay, 2013; Dlugokencky, 2017). Many studies have yielded  
58 reconstructions of Late Cretaceous climates using either climate models or a variety of proxies in  
59 temporally long archives, such as deep-sea cores and continental sections (Pearson et al., 2001;  
60 Huber et al., 2002; Otto-Bliesner et al., 2002; Miller et al., 2003; Friedrich et al., 2012; de Winter et  
61 al., 2014; Vellekoop et al., 2016). Yet, although most deep time climate reconstructions so far have  
62 focused on reconstructing mean annual temperatures (MAT), climate change also involves changes  
63 in other climate parameters, such as precipitation, seasonality and the frequency of extreme  
64 weather events, which all take place on timescales shorter than those that can be resolved in the  
65 above mentioned long archives. Therefore, it is important that these climate variations are  
66 understood on a shorter timescale.

67 One way to achieve such high-resolution palaeoclimate and palaeoenvironmental reconstructions is  
68 by using marine organisms that form shells that grow incrementally. Marine bivalve shells are  
69 excellent palaeoclimate recorders, and the relationship between their shell chemistry and the  
70 environmental conditions in which they grow has been studied intensively (Jones, 1983; Dettman  
71 and Lohmann, 1993; Steuber, 1996; Gillikin et al., 2005a; Elliot et al., 2009). Many geochemical  
72 proxies have been described based on bivalve calcite. Examples include temperature calibrations for  
73 Mg/Ca and stable oxygen isotope ratios ( $\delta^{18}\text{O}$ ; e.g. Klein et al., 1996a; Richardson et al., 2004; Freitas  
74 et al., 2008; Wanamaker et al., 2008), tentative salinity calibrations using Sr/Ca and the combination  
75 of Mg/Ca and  $\delta^{18}\text{O}$  (Dodd and Crisp, 1982; Klein et al., 1996a; Watanabe et al., 2001) and proxies for  
76 palaeoproductivity, such as Ba/Ca and Mn/Ca (Lazareth et al., 2003; Gillikin et al., 2008).

77 Despite their potential for high-resolution palaeoenvironmental reconstruction, bivalve records  
78 feature rarely in long timescale reconstructions (e.g. Steuber, 2005; Harzhauser et al., 2011;  
79 Hallmann et al., 2013). A caveat in the use of bivalve records for long-term palaeoclimate  
80 reconstructions is the potential problems that arise when using multiple bivalve species for  
81 palaeoclimate reconstruction (Gillikin et al., 2005a; b; de Winter et al., 2017a). Culture experiments  
82 in extant bivalve species have shown that palaeoenvironmental proxies in bivalve calcite may be  
83 affected by internal mechanisms that are independent of the environment of the animal and are  
84 controlled by parameters such as growth, reproductive cycle and metabolism (the so-called “vital  
85 effects”; Dunbar and Wefer, 1984; Weiner and Dove, 2003; Gillikin et al., 2005b; Lorrain et al., 2005;  
86 Carré et al., 2005). Such internal factors are often species-specific and limit the applicability of proxy  
87 transfer functions from modern culture studies to multiple species in the same study or on species



88 for which no culture study data is available. The integration of different species of bivalves in  
89 palaeoclimate studies is further complicated by the various ecological niches these species of  
90 bivalves occupy, which results in great variability between their direct environments (Chauvaud et  
91 al., 2005; Dreier et al., 2014). In addition, bivalves are mostly restricted to shallow marine and  
92 estuarine environments. This further complicates the interpretation of bivalve records (e.g. Surge et  
93 al. 2001, Richardson et al., 2004; Gillikin et al., 2008; Wisshak et al., 2009; Ullmann et al., 2010), as  
94 these environments are often characterized by large variations in temperature, salinity and water  
95 chemistry, which makes it hard to disentangle the effect of different environmental parameters on  
96 geochemical proxies (e.g. Duinker et al., 1982; Morrison et al., 1998; Pennington et al., 2000).

97 The above-mentioned problem of combining different high-resolution climate records to study  
98 climatic variations on a geological timescale can be overcome by combining results from multiple  
99 well-preserved bivalve specimens of the same species and in the same geological setting. Several  
100 studies have tried such a multi-specimen approach to trace changes in high-resolution climate  
101 parameters, such as seasonal variations, over geological timescales (Dettman and Lohmann, 2000;  
102 Dettman et al., 2001; Steuber, 2005; Gutiérrez-Zugasti et al., 2016). However, such reconstructions  
103 require bivalve species that preserve well, are geographically widespread, have a high occurrence  
104 frequency over longer timescales and record seasonal-scale variations within their shell.

105 Potential candidate species are bivalves of the genus *Pycnodonte*. This genus of oysters (Bivalvia:  
106 Ostreoida; Fisher von Waldheim, 1835) is characterized by a well-developed commissural shelf and a  
107 vesicular shell structure (hence the name “honeycomb oyster” or “foam oyster”; Stenzel, 1971;  
108 Hayami and Kase, 1992). Members of the genus *Pycnodonte* are found in geological deposits from  
109 the Lower Cretaceous to the Pleistocene. The appearance of *Pycnodonte* shells in a wide range of  
110 palaeolatitudes and geological settings, especially in the Cretaceous, makes them a promising  
111 archive for high-resolution climate reconstruction (Ayyasami, 2006; [Fossilworks, 2017](#)). As  
112 mentioned in Titschak et al. (2010), records from large and long-living bivalves, such as *Pycnodonte*,  
113 provide several advantages in comparison with other seasonality archives. They are slow-growing,  
114 reducing kinetic effects and disequilibrium fractionation of stable isotopes (McConnaughey 1989;  
115 Abele et al., 2009). In addition, *Pycnodonte* bivalves likely did not have symbionts, in contrast to, for  
116 example, Tridacnid bivalves (Elliot et al., 2009). This means that *Pycnodonte* bivalves take up  
117 nutrients and other elements directly from their environment, simplifying the interpretation of their  
118 shell composition. Their low-Mg calcite shells are less prone to diagenetic alteration than shells  
119 made of aragonite or high-Mg calcite (Al-aasm and Veizer, 1986; Pirrie and Marshall, 1990), and their  
120 sedentary life mode ensures that they fossilize in life position. The latter enables the integration of  
121 environmental information extracted from the sediments in which they are fossilized into the  
122 discussion of their shell chemistry.

123 The species *Pycnodonte vesicularis* (Lamarck, 1806) is one of the most common and long-ranging  
124 species of *Pycnodonte*. Therefore, in this study the potential for *P. vesicularis* to be used as a record  
125 for sub-annual environmental variability in the Late Cretaceous is explored. The present study  
126 focuses on the characteristics of fossil specimens of *P. vesicularis* from the upper Maastrichtian  
127 Jagüel Formation of the Bajada de Jagüel section, Argentina (**Figure 1A**). A range of qualitative, semi-  
128 quantitative and quantitative methods are applied to investigate the nature of the *P. vesicularis* shell  
129 material, shell morphology and its preservation state. The aim of this multi-proxy approach is to  
130 characterize the structure and chemical composition of the *P. vesicularis* shell and its development  
131 through the lifetime of the animal and to assess its potential as a recorder of paleoseasonality.

132



## 133 2. The species *Pycnodonte vesicularis*

134 *Pycnodonte vesicularis* was reclining and inhabited muddy bottoms on the shallow marine shelf with  
135 a low sedimentation rate (e.g. Brezina et al., 2014). The individual variability is very extensive in *P.*  
136 *vesicularis*, involving, among others, the outline of valves, their convexity, the thickness of the walls,  
137 the dimensions, the deepness, shape and position of the adductor muscle scar, as well as the  
138 characteristics of chomata (Pugaczewska, 1977; Brezina et al., 2014). This variability depends on the  
139 age of the individual and on local environmental conditions, especially on the character and grain  
140 size of the substrate. According to Berzina et al. (2014), about one third of *P. vesicularis* valves at  
141 Bajada de Jagüel are mature (gerontic) specimens, characterized by relatively thick valves (>10mm)  
142 with a well-developed vesicular layer. Given their longer life span, such mature specimens of *P.*  
143 *vesicularis* were considered most suitable for the present investigation.

144 In the past, several studies have made an attempt to calculate the age of individuals of *P. vesicularis*  
145 based on the number of laminae in the complex of lamellar and vesicular layers (Nestler, 1965), or  
146 the number of growth lines of the ligament (Müller, 1970). Yet, so far no studies have investigated  
147 the potential of *P. vesicularis* shells as palaeoseasonality records based on their geochemical  
148 signature. Given the species-specific relationships between environmental parameters and bivalve  
149 shell geochemistry, in an ideal situation, a culture experiment would be used to determine these  
150 relationships for *Pycnodonte* bivalves. Unfortunately, no extant species of the genus *Pycnodonte* are  
151 known, rendering culture experiments for these species impossible. However, two species of the  
152 closely related pycnodontin genus *Neopycnodonte* (Stenzel, 1971) are found in deep-sea habitats  
153 today (*Neopycnodonte conchlear*, Poli, 1795, and *Neopycnodonte zibrowii*; Videt, 2004; Wisshak et  
154 al., 2009), whereas the extant pycnodontin genus *Hytotissa* is characterized by a shallow-marine  
155 distribution (Titschack et al., 2010). Detailed studies of the shell morphology and chemical  
156 composition of *N. zibrowii* and *Hytotissa hyotis* are reported in Wisshak et al., (2009) and Titschack et  
157 al., (2010), respectively, and can be used as a basis for comparison of the *Pycnodonte* oyster shells.

158

## 159 3. Geological Background

### 160 3.1 Paleogeographical context

161 The studied specimens were collected from the Bajada de Jagüel (BJ) section (38°06'10.5"S,  
162 68°23'20.5"W). The site is situated in the Neuquén Basin in Argentina. The Neuquén Basin is  
163 bordered to the south by the North Patagonian massif and to the northeast by the Sierra Pintada  
164 massif (Figure 1B and 1C). The Bajada de Jagüel section has a palaeolatitude of ~43°S ± 2° relative to  
165 the palaeomagnetic reference frame of Torsvik et al. (2012) according to palaeolatitude.org (van  
166 Hinsbergen et al. 2015). A large transgression from the South Atlantic into the basin (Bertels, 2013)  
167 occurred from the late Maastrichtian to early Danian, during a time of relative tectonic quiescence  
168 and low magmatic activity (Malumian et al., 2011).

### 169 3.2 Palaeoenvironment

170 The Maastrichtian mudstones of the Jagüel Fm are homogeneous and intensely bioturbated,  
171 indicating a well-oxygenated seafloor, with palaeodepths of approximately 50-75 m (Scasso et al.,  
172 2005; Woelders et al., 2017; see also Figure 1). A coarse-grained, mottled, clayey sandstone bed, 15-  
173 25 cm thick, separates the Maastrichtian and Danian mudstones. This sandstone bed represents the  
174 K-Pg boundary and is interpreted to have resulted from a tsunami wave, related to the Chicxulub  
175 impact event (Scasso et al. 2005). During the late Maastrichtian and early Danian, North and Central



176 Patagonia experienced a warm, humid climate. Pollen records suggest rainforests, coastal mangrove  
177 forests and swamp communities in the region (Baldoni 1992; Kiessling et al. 2005; Barreda and  
178 Palazzesi 2007; Iglesias et al. 2007; Palazzesi and Barreda 2007). This vegetation type is classified as  
179 megathermal and indicates average air temperature of 24°C or higher (Barreda and Palazzesi 2007;  
180 Palazzesi and Barreda 2007; Barreda et al. 2012). Average annual sea surface temperatures are  
181 estimated to have been 26-29°C in the latest Maastrichtian at Bajada de Jagüel, based on TEX<sub>86</sub><sup>H</sup>-  
182 palaeothermometry (Woelders et al., 2017; **Figure 1D**). While hypersaline conditions have been  
183 inferred for the northernmost part of the Neuquén Basin, the central part of the Neuquén Basin,  
184 where the BJ site is located, is suggested to have experienced more normal marine conditions. The  
185 latter is evidenced by the presence of planktic foraminifera, dinocysts and relatively few terrestrial  
186 palynomorphs (Prámparo et al. 1996; Prámparo and Papú 2006; Woelders et al. 2017). Yet,  
187 Woelders et al. (2017) inferred enhanced runoff and stratification of the water column at the Bajada  
188 de Jagüel site during the late Maastrichtian warming (450-150 kyr before the K-Pg boundary). Hence,  
189 salinity may have deviated from normal marine during the lifetime of the *Pycnodonte* specimens  
190 studied here.

191

## 192 **4. Materials and methods**

### 193 **4.1 Sample acquisition and preparation**

194 Seven specimens of *Pycnodonte vesicularis* were collected from the upper Maastrichtian Jagüel  
195 Formation in the Bajada de Jagüel section (**Figure 1**), labelled “M0”, “M4”, “M5”, “M6”, “M8”,  
196 “M10” and “M11”. All shells were collected from the upper 5m of below the Cretaceous-Palaeogene  
197 boundary (see **Figure 1**). Four of these specimens (“M0”, “M4”, “M6” and “M11”, see **Figure 2**)  
198 represent completely preserved left valves of mature specimens of *P. vesicularis* (c.f. Pugaczewska,  
199 1977), while the remaining three (“M5”, “M8” and “M10”) were incomplete. Specimens were  
200 selected that differ from each other in morphology, body size and extent of biodegradation, to  
201 assess both the potentials and possible pitfalls of this taxon as a palaeoseasonality recorder. The  
202 four complete shells were cleaned and cast into Araldite® 2020 epoxy resin (Araldite, Basel,  
203 Switzerland) before being cut along the major growth axis of the shell using a slow rotating rotary  
204 saw (Ø 1 mm). A parallel slab was cut out of one half of the shell, while the other half was preserved  
205 (archive half). The resulting thick section, with a typical thickness of 4 mm, was polished using a  
206 series of progressively higher-grade silicon carbide polishing disks (up to P2400) to allow a smooth  
207 surface for sampling and imaging. The remaining three shells were left untreated and were only used  
208 for bulk analysis.

### 209 **4.2 Colour scanning and microscopy**

210 Polished surfaces of shell sections were colour-scanned at 6400 dpi resolution (~4 µm resolution)  
211 using an Epson 1850 flatbed scanner. Shell structures were studied and imaged at 50x magnification  
212 using an Olympus BX60 optical microscope (KU Leuven, Belgium). In order to study the preservation  
213 of pristine calcite in the *P. vesicularis* shells, shell slabs were studied using cathodoluminescence  
214 microscopy using a Technosyn Cold Cathodoluminescence model 8200, mark II microscope operated  
215 at 16-20 kV electron gun potential, 420 µA beam current, 0.05 Torr (6.6 \* 10<sup>-5</sup> bar) vacuum and 5  
216 mm beam width (KU Leuven, Belgium). Cathodoluminescence (CL) refers to the emission of light  
217 from material during excitation by an electron beam. The wavelength (i.e. colour) of the emitted  
218 light depends on the crystal lattice structure and on activators, i.e. light emitting centres constituted  
219 by chemical elements or crystal defects. CL microscopic observations of the shell sections thus



220 enable the recognition of crystal defects and to evaluate the preservation state of the samples (e.g.  
221 overgrowth, recrystallisation, dissolution). They allow to assess to what extent the obtained element  
222 concentrations and isotopic ratios reflect the original shell signature (Barbin, 2000).

#### 223 4.3 Porosity and trace element analysis

224 In order to visualize shell structure and the pore network, high-resolution 3D micro-tomography  
225 analysis was carried out on the archive half of *Pycnodonte* specimens using a General Electric  
226 Nanotom microCT X-Ray CT scanner (KU Leuven, Belgium). One entire shell half was scanned at a  
227 30  $\mu\text{m}$  spatial resolution while representative shell pieces of interest were scanned at 1.5  $\mu\text{m}$   
228 resolution. The CT images were segmented in Matlab by applying a dual thresholding algorithm. The  
229 shell porosity was rendered in 3D and labelled in Avizo Fire 7.0. Pore parameters were calculated in  
230 Avizo and Matlab. Micro-XRF measurements were carried out using a Bruker M4 Tornado micro-XRF  
231 scanner at the XRF platform of the Analytical, Environmental and Geochemistry group at the Vrije  
232 Universiteit Brussel (Brussels, Belgium). Details on the setup of the M4 Tornado  $\mu\text{XRF}$  scanner can be  
233 found in de Winter and Claeys (2016).  $\mu\text{XRF}$  mapping was done using the M4 Tornado's Rh-anode X-  
234 Ray tube under maximum source energy settings (50kV, 600  $\mu\text{A}$ ) using two silicon drift detectors, a  
235 spatial pixel resolution of 50  $\mu\text{m}$  and an integration time of 1 ms per pixel.  $\mu\text{XRF}$  line scans of the  
236 hinges of shells M0, M4, M6 and M11 were measured on the M4 Tornado in point-by-point mode  
237 (see de Winter et al., 2017a) using maximum source energy settings (50kV, 600  $\mu\text{A}$ ), a spot size of 25  
238  $\mu\text{m}$ , a spatial sampling resolution of 50  $\mu\text{m}$  and an integration time per point of 60 seconds (1085  
239 measurements in total). This measurement strategy allowed XRF spectra to accumulate enough  
240 counts to reach the Time of Stable Reproducibility and Accuracy (de Winter et al., 2017b). Line scans  
241 were carried out in growth direction on polished cross sections through the hinge of the four *P.*  
242 *vesicularis* shells (see **Figure 1**). Care was taken to limit sampling to the dense calcite in the hinge of  
243 the shells, though observations of the microstructure of the shell hinge show that incorporation of  
244 vesicular calcite into the profile could not always be avoided (see section 4.1.1 and 4.1.3).

#### 245 4.4 Trace elements in bivalves

246 The use of trace element concentrations in fossil bivalve shells as a means of reconstructing  
247 palaeoenvironmental conditions is subject to ongoing debate. As briefly mentioned above, some  
248 tentative calibrations have been made that link trace element ratios in shell carbonate to  
249 environmental conditions in modern bivalves (e.g. Jones et al., 1980; Klein et al., 1996a; Freitas et  
250 al., 2005; Wanamaker et al., 2008). However, the degree by which the incorporation of these trace  
251 element concentrations is controlled by the shell's environment, as opposed to internal mechanisms  
252 (vital effects), is often uncertain (e.g. Weiner and Dove, 2003; Lorrain et al., 2005; Gillikin et al.,  
253 2005b). An example of this is the Mg/Ca ratio, which is widely thought to reflect the calcification  
254 temperature of the shell (e.g. Klein et al., 1996a). While the Mg/Ca palaeothermometer is commonly  
255 applied in foraminifera studies (e.g. Ederfield and Ganssen, 2000; Lear et al., 2000), calibrations of  
256 this proxy for different bivalve taxa vary widely (Klein et al., 1996a; Vander Putten et al., 2000;  
257 Takesue and van Geen, 2004; Freitas et al., 2005; Wanamaker et al., 2008; Surge and Lohmann,  
258 2008; Mouchi et al., 2013; see also de Winter et al., 2017a). Even Mg/Ca calibration curves for oyster  
259 species within the same genus (*Crassostrea virginica* and *Crassostrea gigas*; Surge and Lohmann,  
260 2008 and Mouchi et al., 2013, respectively) yield very different results, illustrating that the  
261 temperature dependence of Mg/Ca ratios in bivalve calcite is not straightforward. Furthermore, it  
262 has been shown that the incorporation of Mg (and other trace elements, such as Sr and Mn) into  
263 bivalve shells does not happen in equilibrium with ambient concentrations (Weiner and Dove, 2003).  
264 Relationships of bivalve Mg/Ca ratios with temperature are also known to break down during  
265 periods of growth stress (Lorens and Bender, 1980; Takesue and van Geen, 2004). Some Mg in  
266 bivalve shells is associated with organic molecules in the matrix in the shell rather than being



267 substituted for Ca in the crystals of bivalve calcite (Lorens and Bender, 1980). Hence, factors  
268 determining elemental incorporation in bivalve carbonate are partly controlled by physiological  
269 processes and are therefore species specific (e.g. Freitas et al., 2006; 2008).  
270  
271 Another commonly reported ratio, that of Sr/Ca, has yielded good correlations with water  
272 temperature for some bivalve taxa (e.g. Freitas et al., 2005), while others have shown that it strongly  
273 covaries with changes in growth and metabolic rate in a range of taxa (Klein et al., 1996b; Lorrain et  
274 al., 2005; Gillikin et al., 2005b). The above shows that the extent of vital effects is highly taxon-  
275 specific and that climate reconstructions based on trace element records in bivalve shells need to be  
276 interpreted with great care. Beside sea water temperature, attempts have been made to reconstruct  
277 other environmental parameters, such as redox conditions and palaeoproductivity, based on trace  
278 element records in bivalves. Examples of such proxies include elements that are enriched in  
279 skeletons of primary producers such as Ba (Gillikin et al., 2008; Marali et al., 2017), redox-sensitive  
280 elements like Mn (Freitas et al., 2006) and micronutrients such as Zn and Cd, which are known to be  
281 taken up into bivalve shells and whose concentration profiles reflect changes in palaeoproductivity  
282 (Carriker et al., 1980a; Calmano et al., 1993; Jackson et al., 1993; Wang and Fisher, 1996; Guo et al.,  
283 1997). It has been demonstrated that seasonal records of these proxies are reproducible between  
284 different shells in the same environment (Gillikin et al., 2008). While these proxies have not been  
285 explored in detail, their interpretation gives additional information about the ambient sea water  
286 chemistry and illustrates the advantage of applying the multi-proxy approach to reconstruct  
287 seasonality from bivalve shells (de Winter et al., 2017a).  
288

#### 289 4.5 Stable isotope analyses

290 Samples for stable isotope analysis were drilled using a microscope-guided Merchantek drill, coupled  
291 to Leica GZ6 microscope, equipped with a 300 µm diameter tungsten carbide drill bit (AMGC group,  
292 VUB, Belgium). Spatial sample resolutions smaller than the diameter of the drill were obtained by  
293 abrading consecutive samples off the side of the sampling front. This was achieved by moving in  
294 steps of 100µm along a ±2 mm wide linear sampling path, oriented parallel to the growth lines of the  
295 shell and in the growth direction of the shell (447 measurements in total; see also Van Rampelbergh  
296 et al., 2014; Vansteenberge et al., [in review CHEMGEO](#)). Dense foliated calcite in the hinge of the  
297 shells was targeted in sampling for stable isotope analysis, but as a result of the shell structure (see  
298 discussion below) the incorporation of vesicular calcite could not always be excluded. Note that, as a  
299 consequence of the abrading sampling strategy, the width of the sampling path for IRMS samples is  
300 much larger (2 mm) than the width of the sampling path of a µXRF line scan (25 µm). This caused  
301 more vesicular calcite to be incorporated into stable isotope measurements than in µXRF  
302 measurements, as it was easier to avoid the vesicular structure in the µXRF measurements. Aliquots  
303 of ±50 µg of sampled calcite were allowed to react with 104% phosphoric acid (H<sub>3</sub>PO<sub>4</sub>) at 70°C in a  
304 NuCarb carbonate preparation device and stable oxygen and carbon isotope ratios (δ<sup>13</sup>C and δ<sup>18</sup>O)  
305 were measured using a NuPerspective Isotope Ratio Mass Spectrometer (AMGC group, VUB,  
306 Belgium). Analytical uncertainty was determined by repeated measurement (N = 110) of the in-  
307 house reference material MAR2 (Marbella marble, δ<sup>13</sup>C: 3.41 ± 0.10 ‰VPDB; δ<sup>18</sup>O: 0.13 ± 0.20  
308 ‰VPDB; 1 standard deviation, SD) and found to be 0.02‰ and 0.08‰ for δ<sup>13</sup>C and δ<sup>18</sup>O values (1  
309 SD), respectively. This MAR2 reference material was previously calibrated using the international  
310 NBS-19 stable isotope standard (Friedman et al., 1982). All stable isotope values are reported in  
311 permil relative to the Vienna Pee Dee Belemnite standard (‰VPDB). While µXRF and IRMS  
312 measurements were carried out on the same transect, small differences in the length of the records  
313 did occur and these were corrected by linearly rescaling the stable isotope records to match the  
314 length of trace element records in the same shell.



#### 315 4.6 Clumped isotope analysis

316 The stable and clumped isotopic composition of five shells (M4, M5, M8, M10 and M11) was  
317 measured at the University of Michigan Stable Isotope Laboratory. Bulk sampling for clumped  
318 isotope analysis was carried out in two ways: 1) Of three shells (M5, M8 and M10), slabs of dense  
319 calcite were broken off the ventral margin and powdered by hand. 2) Of four shells (M4, M5, M8 and  
320 M11), samples were drilled from the dense hinge area. Sample preparation was performed on a  
321 manual extraction line following Defliese et al. (2015), with the temperature of the Porapak™ trap  
322 increased to avoid fractionating stable isotope values (Petersen et al., 2016). Aliquots of 3.5-5 mg  
323 carbonate powder were reacted with phosphoric acid (H<sub>3</sub>PO<sub>4</sub>) at 75°C and sample CO<sub>2</sub> was analysed  
324 on a ThermoFinnigan MAT253 equipped with Faraday cups to measure m/z 44-49. Each sample was  
325 analysed for 5 acquisitions of 12 cycles each and calibrated relative to heated (1000°C) and H<sub>2</sub>O-  
326 equilibrated (25°C) gas standards and two in-house carbonate standards (Carrara Marble and  
327 Aragonitic Bahamanian Ooids). Gas standards were used to convert unknowns into the absolute  
328 reference frame (Dennis et al., 2011) and carbonate standards (Carrara Marble and Aragonitic  
329 Bahamanian Ooids) were used to quantify reproducibility of reacted samples.  $\delta^{18}\text{O}_{\text{water}}$  values were  
330 calculated using the calcite-H<sub>2</sub>O equation of Kim and O'Neil (1997). External (long term) error on the  
331  $\Delta_{47}$  value was found to be 0.011‰ (1 $\sigma$ ), based on companion measurements of carbonate standards  
332 (see **supplementary data 1**). Data presented in the main manuscript were processed using the  
333 Santrock/Gonfiantini parameters and the high-temperature composite calibration of Defliese et al.  
334 (2015). Further details on the measurement and calibration procedure of clumped isotope  
335 thermometry are found in **supplementary data 1**, along with raw data processed using both  
336 Santrock/Gonfiantini and Brand parameters.

337

### 338 5. Results

#### 339 5.1 *Pycnodonte vesicularis* shell structure

##### 340 5.1.1 Shell microstructures

341 An overview of the results of colour scanning, microscopic analyses and  $\mu\text{XRF}$  mapping on one of the  
342 *P. vesicularis* specimens (M11) reveals the structure of the shells of these honeycomb oysters (**Figure**  
343 **3; supplementary data 3**). A cross section through the shell in direction of maximum growth (**Figure**  
344 **3A**) reveals a layered shell structure with laterally continuous growth increments similar to those  
345 found in modern ostreid shells (e.g. Carriker et al., 1980b; Surge and Lohmann, 2008; Ullmann et al.,  
346 2013). Growth increments are characterized by an alternation of dense, foliated calcite layers with  
347 lighter coloured, more porous, vesicular (“chalky”) calcite layers that are characteristic for the family  
348 Gryphaeidae (Linnaeus, 1758; Carriker et al., 1980b; Bieler et al., 2004; Surge and Lohmann, 2008).  
349 The porosity in these vesicular layers is visualized in microscopic images (**Figure 3C-E**). Microscopic  
350 images also show that the hinge of the shell is mostly devoid of this vesicular structure, and instead  
351 consists of a close packing of foliated calcite layers (**Figure 3A** and **Figure 3G**). However, in parts of  
352 the hinge small layers of vesicular calcite are also visible between the foliated layers in **Figure 3G**. In  
353 places where these vesicular layers are interlocked between foliated layers, the transition between  
354 the two microstructures is gradual. Microscopic images (**Figure 3D-E**) show that farther away from  
355 the shell hinge, the transitions between foliated calcite and vesicular calcite are sharp, and that  
356 individual layers of foliated and chalky calcite can be very thin (<30  $\mu\text{m}$ ; **Figure 3D**). Pores in the  
357 vesicular calcite are heterogeneous in size and can be up to 200  $\mu\text{m}$  wide. While the shell structure is  
358 in general very well preserved (**Figure 3C-G**), it is disturbed in some areas by patches of different





359 texture, or holes that have been previously ascribed to boring polychaete worms (Brezina et al.,  
360 2014).

### 361 5.1.2 Porosity

362 Micro-CT images of one of the *P. vesicularis* specimens (M4) further illustrate the distribution of  
363 porosity in the shell (**Figure 4**). Porosity analysis based on micro-CT scanning confirms the  
364 microscopic observations of porous vesicular calcite and dense foliated calcite layers in the shells.  
365 Quantitative analyses of porosity through the shell (porosity logs) on the high-resolution CT scan of a  
366 small part of the shell (**Figure 4B**) shows that the distribution of porosity strictly relates to growth  
367 layering of the shell. The porosity log perpendicular to the growth layering (**Figure 4E**) shows that  
368 porosity is almost absent in the foliated calcite layers and reaches up to 65% of the shell volume in  
369 the most porous vesicular layers. Total shell CT scan results reveal that the average porosity in the  
370 shell is 21%. Results of CT scanning and microscopy show that, while the calcite in the vesicular  
371 microstructure was affected by diagenesis, the original porosity in these *P. vesicularis* shells has been  
372 preserved almost completely, and the filling of pores by recrystallized calcite is relatively uncommon  
373 (see **Figure 3D-E**).

### 374 5.1.3 Chemical heterogeneity and cathodoluminescence

375 Heterogeneity in the *P. vesicularis* shell is also evidenced by the distribution of iron (Fe) and  
376 manganese (Mn) in the shell, as illustrated by  $\mu$ XRF mapping (**Figure 3B**). The map shows that the  
377 vesicular layers in the shell are characterized by higher concentrations of Fe and Mn than the dense  
378 foliated calcite layers. Parts of the shell that were perforated by bore holes have especially high  
379 concentrations of Fe and Mn, and these holes are surrounded by a corona of elevated Fe and Mn  
380 concentrations (**Figure 3H and I**). A close-up of the shell hinge in **Figure 3B** confirms that it consist  
381 almost entirely of dense foliated calcite with low Fe and Mn concentrations. The same close-up also  
382 illustrates the limitations of  $\mu$ XRF mapping with a spot size of 25  $\mu$ m. The method is not able to  
383 resolve variations in the concentration of Fe and Mn on the scale of fine (<30  $\mu$ m) laminations in the  
384 shell hinge. A composite of cathodoluminescence microscopy images of the same area (insert in  
385 **Figure 3A**) complements  $\mu$ XRF mapping by showing in more detail that the foliated calcite of the  
386 shell hinge is characterized by microscopic growth increments that show a dull luminescence. Only  
387 the largest increments can be distinguished on the  $\mu$ XRF map. In calcite,  $Mn^{2+}$  is the main  
388 luminescence activator causing emission of yellow to orange light (~620 nm; Machel and Burton,  
389 1991) of which the intensity is positively correlated with the Mn concentration (de Lartaud et al.,  
390 2000a; Habermann, 2002; Langlet et al., 2006; de Winter and Claeys, 2016). Indeed, brighter layers  
391 in the CL image correspond with higher Mn values in the XRF map. An enlarged version of the CL  
392 composite shown in **Figure 3** is given in **supplementary data 2** and XRF Mn and Fe maps of all shells  
393 are given in **supplementary data 3**.

### 394 5.2 Trace element profiles

395 Results of XRF line scans through all *P. vesicularis* shells featuring in this study are given in  
396 **supplementary data 4**. Quantitative XRF line scans through the hinge of the *P. vesicularis* shells yield  
397 records of [Ca], [Si], S/Ca, Zn/Ca, Sr/Ca, Mg/Ca, [Mn] and [Fe] in growth direction through the dense  
398 hinge area of the shells (**Figure 5**). All measured XRF data is directly represented in **Figure 5**, only the  
399 Mg/Ca record is plotted with a three point running average. This running average smooths out the  
400 variation between individual Mg/Ca measurements, because Mg is slightly more susceptible to  
401 interferences on the XRF spectrum, causing noise on the Mg/Ca record. This results from the fact  
402 that Mg is on the edge of the spectrum of elements measurable by the M4 Tornado  $\mu$ XRF scanner



403 and is therefore (see de Winter and Claeys, 2016; de Winter et al., 2017b). A plot of these results  
404 shows that concentrations of calcium (Ca) and silicon (Si) in all shells generally remain above 38  
405 mass% and below 0.5 mass%, respectively. In three out of four specimens (M0, M4 and M6),  
406 absolute concentrations of Fe and Mn rarely exceed 800  $\mu\text{g/g}$  (**Figure 5**). The exception is the iron  
407 record of specimen M11, which shows maxima often exceeding 2000  $\mu\text{g/g}$ . Fe concentrations in M6  
408 are also elevated in comparison with M0 and M4, leading to the suggestion that there might be a  
409 link between the presence of bore holes (observed in M6 and M11) and elevated Fe-concentrations.  
410 A cross plot in **Figure 6A** shows that the concentrations of Fe and Mn are weakly correlated in XRF  
411 line scan measurements. Furthermore, samples with elevated concentrations of Mn generally have  
412 lower concentrations of Sr, especially when Mn concentrations are higher than 800  $\mu\text{g/g}$  (**Figure 6B**).  
413 Both are a sign of diagenetic alteration because Mn and Fe have been shown to be preferentially  
414 enriched in recrystallized shell carbonates, while Sr is preferentially removed during the  
415 recrystallisation process (Brand and Veizer, 1980; Al-Aasm and Veizer, 1986). Trace element profiles  
416 through the four *P. vesicularis* specimens show that there is a good overall agreement between  
417 shells both in terms of absolute concentration of magnesium (Mg), strontium (Sr), zinc (Zn) and  
418 sulphur (S) and their internal variation. Records of ratios of Mg/Ca, Sr/Ca, Zn/Ca and S/Ca show  
419 quasi-cyclic oscillations. In records of Mg/Ca and Sr/Ca, these oscillations are quasi sinusoidal, while  
420 records of Zn/Ca and S/Ca are characterized by short-lived increases relative to a baseline value.  
421 Trace element ratios generally oscillate around a stable baseline value, though in some cases (e.g.  
422 Sr/Ca and Mg/Ca in M11) there is a slight evolution of this baseline value in the direction of growth.

### 423 5.3 Stable isotope analysis

#### 424 5.3.1 Stable isotope records

425 Records of stable oxygen isotope ratios ( $\delta^{18}\text{O}$ ) and stable carbon isotope ratios ( $\delta^{13}\text{C}$ ) are plotted  
426 together with trace element ratios in **Figure 5**. As in the trace element records, absolute values as  
427 well as internal variation of stable isotope records show good agreement between shells. Values in  
428 the  $\delta^{18}\text{O}$  record oscillate around a baseline value of  $-1.5\text{‰}$ . The  $\delta^{13}\text{C}$  baseline values are a bit more  
429 variable, possibly showing a late ontogenetic trend in M6, but remaining stable at  $2\text{‰}$  in the other  
430 specimens. Stable oxygen isotope ratios remain between  $-2.5\text{‰}$  and  $-0.5\text{‰}$  for the majority of the  
431 records, exceptions being  $\delta^{18}\text{O}$  values below  $-3\text{‰}$  in a few measurements in M4, the central part of  
432 the M6 record, and a few measurements in the youngest part of the M0 record. Similarly,  $\delta^{13}\text{C}$  ratios  
433 in all shells remain between  $1.5\text{‰}$  and  $3.5\text{‰}$ , except for the latter cases. Cross plots between  
434 isotope ratios show that samples with exceptionally low  $\delta^{18}\text{O}$  values ( $<-3\text{‰}$ ) often also exhibit  
435 decreased  $\delta^{13}\text{C}$  values ( $<1.5\text{‰}$ ; **Figure 6D**). This relationship between  $\delta^{18}\text{O}$  and  $\delta^{13}\text{C}$  values is  
436 significant in shells M4, M6 and M11, and not in M0. Such a relationship between  $\delta^{18}\text{O}$  and  $\delta^{13}\text{C}$  has  
437 often been interpreted as a sign of diagenetic alteration. Therefore, the absence of this relationship  
438 in M0 in contrast to the other shells shows that the stable isotope profile from the hinge of shell M0  
439 is least affected by diagenetic alteration. Stable oxygen and carbon isotope records seem to show  
440 quasi-periodic variations around these baseline values, with amplitudes of about  $1\text{‰}$  and  $0.5\text{‰}$   
441 respectively (**Figure 5**). Cross plots of proxy records show that  $\delta^{18}\text{O}$  and  $\delta^{13}\text{C}$  values are generally  
442 lower in samples with elevated concentrations of Mn and Fe (**Figure 6A and 6C**).

#### 443 5.3.2 Clumped isotope analysis

444 Clumped isotope analyses of ventral margin calcite from three *P. vesicularis* shells from the same  
445 locality (M5, M8 and M10) yielded  $\Delta_{47}$  values of 0.699 to 0.707 $\text{‰}$ , equivalent to a temperature range  
446 of 21–25°C using the high temperature composite calibration of Defliese et al., 2015 (see **Table 1**).  
447 Both reconstructed temperatures and  $\delta^{18}\text{O}_{\text{seawater}}$  values varied significantly between these samples,



448 with  $\delta^{18}\text{O}_{\text{seawater}}$  ranging from -0.6‰ in M10 to -2.2‰ and -5.9‰ in M5 and M8 respectively, likely  
449 indicating the influence of altered calcite material. This is supported by shell  $\delta^{18}\text{O}$  values, which  
450 deviate to very low values (-4‰ to -7‰VPDB in M5 and M8) well outside of the range of samples  
451 micromilled from the well-preserved hinge carbonate (**Figure 5**). The same samples (M5 and M8)  
452 also show relatively decreased  $\delta^{13}\text{C}$  values (<1‰), further indicating that these decreased stable  
453 isotope ratios are likely indicative of diagenetic alteration. In comparison, samples of the dense  
454 hinge calcite from M4, M5, M8 and M11, yielded  $\delta^{18}\text{O}_{\text{seawater}}$  values ranging from -1.8‰ to -2.5‰  
455 and  $\Delta_{47}$  values of 0.725 to 0.746‰, corresponding to much cooler temperatures of 9-15°C. Shell  $\delta^{13}\text{C}$   
456 and  $\delta^{18}\text{O}$  values from bulk samples of hinge carbonate resemble values measured in the high-  
457 resolution transects, further supporting the good preservation of carbonate in this area.

458

## 459 6. Discussion

### 460 6.1 Shell preservation

#### 461 6.1.1 Visualization of diagenesis

462 The preservation of fine shell porosity measured by CT-scanning shows that if any recrystallization  
463 occurred in the shells, it was not so extensive that the pores in the vesicular layers were filled by  
464 secondary calcite. Yet, identifying diagenesis in *P. vesicularis* shells cannot be done based on simple  
465 visual inspection alone. Recrystallized calcite is often characterized by elevated concentrations of  
466 Mn and Fe, which are released into pore waters of the sediment surrounding the shell under  
467 reducing conditions (Al-Aasm and Veizer, 1986). This allows the distribution of Fe and Mn  
468 concentrations in the shells to be used as an indicator for the amount of recrystallization and the  
469 preservation of the shell. The map in **Figure 3B** shows that such recrystallization is predominantly  
470 observed in the vesicular calcite and that Fe and Mn concentrations in foliated calcite layers are low.  
471 Coronas of elevated Fe and Mn concentrations around the bore holes in the shells confirm that  
472 increased concentrations of Mn and Fe are leached into the shell through these holes as penetrating  
473 pore fluid carrying these ions can more easily infiltrate the vesicular calcite layers than the foliated  
474 calcite. The fact that shells M6 and M11, which contain the most bore holes (see **Figure 2**), have the  
475 highest Mn and Fe values (**Figure 5**) supports this hypothesis. This pattern is confirmed by the  
476 cathodoluminescence microscopy images, which show minimal dull luminescence in the foliated  
477 calcite, indicative of limited contamination of the calcite by Mn and Fe (Barbin, 2000). Thin lamina  
478 between foliated calcite layers show brighter luminescence, associated with higher concentrations  
479 of Fe and Mn. This is in agreement with peaks in Mn and Fe observed in the  $\mu\text{XRF}$  profiles of M11  
480 (**Figure 5**). Microscopic images of the foliated calcite structure (e.g. **Figure 3F-G**) further show that  
481 the elongated crystal structure characteristic of pristine foliated shell calcite has not been  
482 compromised by diagenesis (Ullmann et al., 2010). Comparison between the CL composite and the  
483  $\mu\text{XRF}$  map shows that, while  $\mu\text{XRF}$  mapping does pick up large scale diagenetic features in the shell,  
484 it fails to reveal most of the small layers intercalated between foliated calcite layers in the shell  
485 hinge because they are smaller than the spot size of the  $\mu\text{XRF}$  scanner (25  $\mu\text{m}$ ). This illustrates that  
486  $\mu\text{XRF}$  mapping is a useful tool for screening for diagenesis, but fails to pick up the fine details that  
487 are visualized by CL-microscopy. Similarly, Mn and Fe profiles in  $\mu\text{XRF}$  line scanning will miss or  
488 average out the small layers of vesicular calcite present in some parts of the shell hinges of *P.*  
489 *vesicularis* and CL-microscopy remains a necessary tool for thorough screening for diagenesis.

#### 490 6.1.2 Diagenesis in trace element profiles



491 Quantitative XRF line scans through the hinge of the *P. vesicularis* specimens show that absolute  
492 concentrations of Fe and Mn rarely exceed 800  $\mu\text{g/g}$  in all shells except for M11 (**Figure 5**). While Mn  
493 concentrations measured in the hinges of *P. vesicularis* are higher than is considered typical for well-  
494 preserved bivalve calcite and often exceed the diagenesis threshold of 300  $\mu\text{g/g}$  proposed by  
495 Steuber (1999), high concentrations of Sr (>700  $\mu\text{g/g}$ ) and Mg (>1000  $\mu\text{g/g}$ ), comparatively low Fe  
496 concentrations and the observation of non-luminescent, well-preserved foliated calcite crystals  
497 (**Figure 3**) suggest preservation of the original trace element signature (Veizer, 1983; Al-Aasm and  
498 Veizer, 1986; Steuber, 1999). The peaks of high Fe concentrations in the M11 shell and elevated Fe  
499 concentrations in M6 compared to the other shells coincide with decreases in  $\delta^{18}\text{O}$  and  $\delta^{13}\text{C}$ . In  
500 general, stable isotope values are lower in intervals of the records characterized by elevated levels of  
501 Mn and Fe that exceed the baseline variation. Similarly, concentrations of Sr are generally lower in  
502 samples with higher Mn concentrations (**Figure 6B**). This trend is especially clear in samples of which  
503 Mn concentrations exceed 800  $\mu\text{g/g}$ . This suggests that in these specimens of *P. vesicularis*, Fe and  
504 Mn concentrations exceeding 800  $\mu\text{g/g}$  likely signify areas where recrystallization has occurred (see  
505 also **Figure 6A-C**). We therefore propose 800  $\mu\text{g/g}$  as a tentative maximum threshold for the  
506 preservation of pristine calcite in shells of *P. vesicularis* in this setting, and consider samples  
507 exceeding this threshold in concentration for either Mn or Fe as diagenetically altered. Except for a  
508 few measurements in shells M6 and M11, low Si concentrations and high Ca concentrations in the  
509 trace element records shown in **Figure 5** indicate limited incorporation of detrital material into the  
510 hinge of the shell (see de Winter and Claeys, 2017; de Winter et al., 2017a). This shows that the  
511 infills of bore holes by detrital material have not significantly influenced the chemical signal of the  
512 hinges of the shells. Indeed, the locations of these bore holes away from the shell hinge are  
513 observed in **Figure 2 and 3**. From this it follows that the majority of post-mortem alteration of the  
514 shells occurred through the process of chemical alteration (e.g. recrystallization) rather than physical  
515 processes (e.g. predatory burrowing). As described above (see 5.1.1), the role of bore holes in the  
516 shells (especially M6 and M11) in the diagenetic process was predominantly to provide entries  
517 through which pore waters could enter to cause recrystallization. Bore holes elsewhere in the shells  
518 may lead to migration of fluids through the shell, ultimately resulting in elevated concentrations  
519 throughout the shell.

### 520 6.1.3 Diagenesis in stable isotope records

521 The majority of the stable isotope ratios measured the shell records are in agreement with those of  
522 well-preserved Low Magnesium Calcite (LMC) of fossil (Steuber, 1996; 1999; Tripathi et al., 2001) and  
523 modern marine mollusc shells (Klein et al., 1996a;b; Goodwin et al., 2001; Lécuyer et al., 2004). The  
524 low  $\delta^{18}\text{O}$  and  $\delta^{13}\text{C}$  values characterizing the central part of the M6 shell hinge record is an exception  
525 to this and these values are likely explained by incorporation of vesicular calcite into the micromilled  
526 samples. It is evident from the scan image of M6 in **Figure 2** how an extension of this shell mineral  
527 phase into the umbo has resulted in the sampling of vesicular calcite in the centre of the record. The  
528 resulting sudden decrease in  $\delta^{18}\text{O}$  and  $\delta^{13}\text{C}$  towards values below -4‰ and 1‰ respectively (a drop  
529 of 2-3‰ for  $\delta^{18}\text{O}$  and 1-2‰ for  $\delta^{13}\text{C}$ ) illustrates that stable isotope composition of this vesicular  
530 calcite deviates significantly from that of the foliated calcite. Similarly, the record from specimen M4  
531 also has several stable isotope samples that most likely contain vesicular calcite. Lobes of vesicular  
532 calcite in this specimen extend close to the hinge line, making incorporation of this microstructure  
533 more likely. Several samples in the isotopic record of M4 are indeed characterized by unusually low  
534 isotopic values. We consider it likely that small amounts of vesicular calcite were incorporated in  
535 these samples.



536 The exceedingly low  $\delta^{18}\text{O}$  values in some samples from the vesicular calcite suggests that the original  
537 composition is either not preserved due to alteration or that this vesicular calcite was initially  
538 precipitated in disequilibrium with respect to ambient sea water (Grossman and Ku, 1986; Woo et  
539 al., 1993; Steuber, 1999). The latter could be in agreement with the hypothesis that vesicular  
540 structures in oyster shells are formed by microbes instead of by the bivalve itself (Vermeij, 2014).  
541 However, microscopic images of the vesicular structure reveal blocky calcite crystals in some areas  
542 (**Figure 3D**), which suggest recrystallization (e.g. Folk and Land, 1975; Schlager and James, 1978).  
543 Indeed, the offset in stable isotope ratios of vesicular calcite compared to foliated calcite is not  
544 found in modern oyster shells (Surge and Lohmann, 2008; Ullmann et al., 2010), and is therefore  
545 most likely a result of preferential diagenetic alteration of the vesicular calcite. Elevated Mn and Fe  
546 concentrations found in XRF mapping (**Figure 3**), and the notion that similar chalky or vesicular  
547 phases in modern oyster shells are less crystalline and grow faster (Chinzei and Seilacher, 1993;  
548 Ullmann et al., 2010), further attest to the fact that vesicular calcite in *P. vesicularis* (and likely in  
549 other fossil members of the Gryphaeidae) is more prone to diagenetic alteration than its foliated  
550 counterpart, and therefore provides no suitable record of palaeoclimatic information.

551 This conclusion is also supported by the clumped isotope analysis results. Bulk samples from the  
552 ventral margin of the shell (containing more vesicular calcite, see **Figure 2 and 3**) contain lower  
553 stable isotope ratios and higher reconstructed temperatures than samples from the dense shell  
554 hinge (**Table 1; Figure 7**). Elevated temperatures in these samples likely reflect recrystallization of  
555 shell material from slightly warmer pore fluids after burial. However, temperatures from diagenetic  
556 samples (average = 23°C) are relatively low compared to typical pore fluid temperatures measured  
557 from diagenetic calcite in other studies (30-120°C; Huntington et al., 2011; Loyd et al., 2012; Dale et  
558 al., 2014). Together with the fact that the difference between altered and unaltered samples (23°C  
559 vs. 11°C; **Table 1**) is relatively small and that the dense calcite portions seem to be unaffected by  
560 diagenesis, which suggests that burial was shallow. The shallow burial history is also demonstrated  
561 by the preservation of organic biomarkers in the Bajada de Jagüel section (Woelders et al., 2017).

#### 562 **6.1.4 Implications for sampling strategy**

563 Contrary to what may be expected based on the XRF map of M11 in **Figure 3**, the incorporation of  
564 vesicular calcite into the microdrilled samples of M6 is not always reflected in elevated Mn and Fe  
565 concentrations in the  $\mu\text{XRF}$  line scans. This could suggest that trace element signatures in vesicular  
566 calcite this close to the shell hinge are not strongly affected by the leaching of reducing pore waters  
567 that likely elevated the concentrations of these elements in the vesicular calcite of the rest of the  
568 shell. Alternatively, it is likely that more of the vesicular calcite was incorporated in the microdrilled  
569 samples for stable isotopes, than in the XRF line scan, as the line scan is only 25  $\mu\text{m}$  wide and  
570 relatively close to the hinge line, whereas the linear sampling paths of the microdrilling covered a  
571 much larger area (up to 2 mm wide parallel to the growth increments). The wide sampling line  
572 needed to sample for stable isotope analysis at this spatial resolution (100  $\mu\text{m}$  in the direction of  
573 growth) increases the chance of incorporating vesicular calcite into the samples, particularly in  
574 samples further away from the hinge line and in shells where vesicular calcite layers penetrate close  
575 to the hinge line (e.g. M4 and M11, see **Figure 2, Figure 3 and Figure 6D**). This result illustrates a  
576 disadvantage of the abrasion-style microdrilling method applied in this study for spatially  
577 heterogeneous bivalves. It shows that thorough screening for diagenesis using both trace element  
578 analysis and cathodoluminescence is essential to correctly interpret the stable isotope results.

579 Summarizing, shells M6 and M11 are characterized by elevated Fe and Mn concentrations in the  
580 shell hinge line, signifying that these specimens contain larger amounts of recrystallized vesicular  
581 calcite in their shell hinge. Specimen M4 shows lower Fe and Mn concentrations in the shell hinge,



582 but low stable isotope ratios show that several microdrilled samples contain diagenetically altered  
583 vesicular calcite. Stable carbon and oxygen isotope ratios in shells M4, M6 and M11 all show a  
584 significant positive relationship, while such a relationship is absent in M0. As a result, of the 4  
585 specimens investigated, specimen M0 is considered to represent the best preserved specimen, most  
586 likely providing the most reliable results in terms of palaeoenvironmental reconstruction. Coloured  
587 vertical bars in **Figure 5** illustrate parts of the shell records that were considered diagenetically  
588 altered based on one or more of the criteria described above: 1) Bright luminescence in CL-  
589 microscopy. 2) elevated (>800 µg/g) Fe and/or Mn concentrations. 3) Elevated Si (>0.5 mass%) and  
590 reduced Ca (<38 mass%) concentrations. 4) Decreased stable isotope ratios ( $\delta^{18}\text{O} < -3\%$  and  $\delta^{13}\text{C} <$   
591  $1.5\%$ ).

## 592 **6.2 Periodic variations**

### 593 **6.2.1 Shell chronology**

594 While earlier studies have been successful in determining the chronology of geochemical records  
595 from comparatively young (Quaternary) fossil bivalves (e.g. Scourse et al., 2006; Marali and Schöne,  
596 2014), attempts at palaeoseasonality reconstruction based on more ancient (pre-Quaternary) shells  
597 have shown that this is not straightforward (Dettmann and Lohmann, 1993; Bougeois et al., 2014; de  
598 Winter and Claeys, 2016; de Winter et al., 2017a). Quasi-periodic variations in stable oxygen  
599 isotopes, Sr/Ca ratios and Mg/Ca ratios seem to represent seasonal cycles in shell growth (**Figure 5**),  
600 but on closer inspection it is difficult to find a consistent phase relationships between these records  
601 through all four shells. The most well-preserved shell record (M0) was tentatively subdivided into  
602 annual cycles based on Sr/Ca and  $\delta^{18}\text{O}$  seasonality. **Figure 8** shows a stack of the trace element  
603 records created based on these subdivisions. Similar year stacks of the other three shells yielded  
604 different phase relationships between proxies (**supplementary material**). These differences are  
605 likely explained by the incorporation of diagenetically altered vesicular calcite in some of the  
606 microdrilled samples, resulting in significantly lighter carbon and oxygen isotopic values. Especially in  
607 the record of shell M4 (**Figure 5**), it is clear how diagenesis can preferentially influence one season  
608 over the other and result in a change of the phase relationship between proxies in the shell. In the  
609 case of M4, the incorporation of lobes of vesicular calcite into the shell hinge seems to be paced to  
610 the seasonal cycle, making it difficult to disentangle patterns in diagenetic alteration from seasonal  
611 patterns in the shell records. The incorporation of diagenetically altered vesicular calcite into the in  
612 the shell hinge has influenced stable isotope profiles in shells M4, M6 and M11 more than M0, as is  
613 evident from the significant correlation between  $\delta^{18}\text{O}$  and  $\delta^{13}\text{C}$  in these shells, which is absent in M0  
614 (**Figure 6D**). Such preferential incorporation of vesicular calcite into the hinge during one season can  
615 occur when the bivalve experiences more physiological stress in that season (Müller, 1970). Indeed,  
616 even when diagenetically altered parts of these records (according to the threshold of 800 µg/g for  
617 Fe and Mn and  $-3\%$  for  $\delta^{18}\text{O}$ ) are excluded, seasonal patterns in year stacks of shells M4, M6 and  
618 M11 do not fully agree with those in the better preserved M0 shell. This leads to the assumption  
619 that poorer preservation prevents the establishment of a reliable chronology for these shells. That  
620 said, records from shells M4, M6 and M11 should not be dismissed, as variation in the geochemical  
621 proxies measured in pristine parts of these shells could still yield valuable information about the  
622 extent of seasonality during their growth, even though phase relationships are blurred by diagenetic  
623 overprinting. The fact that stable isotope measurements in these shells were not taken from the  
624 exact same location as trace element measurements (due to different sampling and measurement  
625 techniques) further complicates the establishment of consistent phase relationships between  
626 geochemical records in the shells. The most obvious way in which this affected phase relationships  
627 between records is the fact that stable isotope samples were more severely laterally averaged (2



628 mm wide transect compared to 25  $\mu\text{m}$  wide transect of  $\mu\text{XRF}$  measurements), and the fact that  
629 stable isotope records were rescaled to the length of XRF records before being plotted in **Figure 5**  
630 (see section 4.5).

### 631 **6.2.2 Phase relationships**

632 Since only one of the shells measured in this study (M0) showed good enough preservation for a  
633 discussion of phase relationships between records, care must be taken in extrapolating the  
634 conclusions drawn from the year stack of this single shell. However, a tentative discussion of these  
635 phase relationships may still shed some light on the mechanisms that drive the incorporation of  
636 these proxies into the shell of *P. vesicularis*. The year stack of the well-preserved specimen M0  
637 (**Figure 8**) shows that the  $\delta^{18}\text{O}$ ,  $\delta^{13}\text{C}$  and Sr/Ca records exhibit a sinusoidal pattern with one peak per  
638 year. In contrast, records of Zn/Ca, S/Ca and Mg/Ca contain a double peak in each year. Comparing  
639 these observations with the records in **Figure 5** shows that the same seems to be true for the  
640 pristine parts of the other three shells. In addition, the M0 year stack shows that maxima in  $\delta^{13}\text{C}$   
641 ratios coincide with minima in Sr/Ca and Zn/Ca and that minima in  $\delta^{18}\text{O}$  ratios follow maxima in  $\delta^{13}\text{C}$   
642 after about one quarter of an annual cycle. Zn/Ca and S/Ca records show an antiphase relationship,  
643 and the Mg/Ca record has one minimum that coincides with a minimum in  $\delta^{18}\text{O}$  ratios and another  
644 half a cycle earlier.

### 645 **6.3 Interpreting geochemical records in *Pycnodonte vesicularis***

#### 646 6.3.1 Comparison with other taxa

647 Carbon isotope values found in this study are higher than in oysters living in modern coastal  
648 temperate environments (Surge et al., 2001; Ullmann et al., 2010), but more similar to oysters living  
649 in warmer, high-salinity or tropical settings (Klein et al., 1996a; Surge and Lohmann, 2008; Titschack  
650 et al., 2010). Oxygen isotope ratios are generally lower than modern coastal mid latitude bivalves  
651 (Ullmann et al., 2010; Klein et al., 1996b) and in better agreement with warmer, low latitude studies  
652 (Lécuyer et al., 2004) and other Cretaceous bivalves (Steuber, 1999). This is in agreement with  
653 reconstructions of  $\delta^{18}\text{O}$  ratios in Late Cretaceous oceans that were  $\sim 1\%$  lower compared to the  
654 present-day ocean due to the absence of extensive polar ice sheets in the Late Cretaceous (e.g. Hay,  
655 2008). These results are in agreement with the warmer palaeoenvironmental setting inferred for the  
656 Late Cretaceous of Neuquén Basin, based on  $\text{TEX}_{86}$ -palaeothermometry (Woelders et al., 2017).  
657 However, the clumped isotope thermometry results of this study suggests rather cooler  
658 temperatures. In order to properly interpret geochemical records from *P. vesicularis*, it is important  
659 to compare the results of this study with those from closely related bivalves. Although the genus  
660 *Pycnodonte* has no living members, two sister taxa in the subfamily Pycnodontinae (Stenzel, 1959)  
661 contain extant members: *Hyotissa* and *Neopycnodonte* (Stenzel, 1971).

#### 662 6.3.2 *Hyotissa hyotis*

663 The microstructure of *Hyotissa hyotis* is similar to that of *P. vesicularis*, with porous vesicular phases  
664 alternated with dense foliated calcite layers. A specimen of *Hyotissa hyotis* in the northern Red Sea  
665 was subject to a stable isotope study by Titschack et al. (2010). That study illustrates that, in contrast  
666 to what was argued by Nestler (1965), the microstructure alternations in pycnodontin bivalves do  
667 not correlate to annual growth increments. In the specimen of *H. hyotis* (Titschack et al., 2010),  
668 seasonal variations in  $\delta^{18}\text{O}$  and  $\delta^{13}\text{C}$  were found to be independent of shell microstructure. Similarly,  
669 in modern oysters like *Crassostrea virginica* (Surge and Lohmann, 2008) and *Crassostrea gigas*  
670 (Ullmann et al., 2010), no isotopic difference is observed between different shell microstructures  
671 (foliated vs vesicular calcite). This may explain why year stacks of *P. vesicularis* shells that were



672 affected by diagenesis differ from those of the well-preserved M0 specimen. The isotopically lighter  
673 values observed in the vesicular calcite of *P. vesicularis* result from recrystallization, not of annual  
674 cyclicity, and this incorporation of diagenetically altered samples into the record disturbed the  
675 original stable isotope seasonality. Stable carbon isotope ratios in *H. hyotis* are very similar to those  
676 measured in *P. vesicularis*. In principle, the  $\delta^{13}\text{C}$  signal of shells is controlled by the  $\delta^{13}\text{C}$  value of the  
677 dissolved inorganic carbon (DIC) of the organism's extrapallial Fluid (EPF), from which the shell is  
678 precipitated (Kirby, 2000). In marine bivalves, the carbon isotope composition of the EPF is  
679 controlled by the  $\delta^{13}\text{C}$  of ambient seawater, carbonate ion effects, pH, food availability, growth,  
680 valve gape/closure intervals, and seasonal changes in metabolic rate (Romanek et al. 1992;  
681 McConnaughey et al. 1997; Kirby et al. 1998; Owen et al. 2002; Geist et al. 2005; McConnaughey and  
682 Gillikin, 2008; Lartaud et al. 2010b). All these processes vary in strength and time, which complicates  
683 interpretation of the  $\delta^{13}\text{C}$  signal (Lorrain et al. 2004; Omata et al. 2005). According to Titschack et al.  
684 (2010),  $\delta^{13}\text{C}_{\text{shell}}$  of *H. hyotis* is most strongly controlled by bivalve respiration, which is increased  
685 during periods of enhanced planktonic food supply. They recorded a shifted phase relationship  
686 between  $\delta^{18}\text{O}$  and  $\delta^{13}\text{C}$  records in *H. hyotis* similar to the phase shift observed in **Figure 8**, which was  
687 attributed to phase-shifted cycles in sea surface temperature and productivity. In *H. hyotis* there is  
688 an anti-phase relationship between  $\delta^{13}\text{C}$  and daily sunshine hours, suggesting that in our records of  
689 the closely related *P. vesicularis*, the lowest annual  $\delta^{13}\text{C}$  values likely correspond to mid-summer  
690 (December).

### 691 6.3.3 *Neopycnodonte zibrowii*

692 A specimen of *Neopycnodonte zibrowii* (Videt, 2004) was subject to detailed multi-proxy analysis in  
693 Wisshak et al. (2008). This large, deep dwelling (450–500m) bivalve from the Azores shows similar  
694 alternations in vesicular and foliated calcite as *P. vesicularis*, but has a much longer lifespan. Trace  
695 element records in *N. zibrowii* show much higher Mg/Ca and S/Ca and lower Sr/Ca ratios compared  
696 to those found in *P. vesicularis* in this study. Consecutive peaks in Mg/Ca and S/Ca coinciding with  
697 minima in Ca and Sr concentration in this shell are interpreted as a sign of a strong control of growth  
698 and reproductive cycle on trace element ratios. The covariation of Mg/Ca and S/Ca records in bivalve  
699 calcite has often been interpreted as evidence of internal control on trace element concentrations  
700 rather than external forcing (e.g. by temperature; Lorens and Bender, 1980; Rosenberg and Hughes,  
701 1991). Such relationships between Mg/Ca, S/Ca and Sr/Ca are, however, not observed in *P.*  
702 *vesicularis* (**Figure 5**, **Figure 6** and **Figure 7**). While  $\delta^{13}\text{C}$  values in *N. zibrowii* are similar to those  
703 found in this study,  $\delta^{18}\text{O}$  in *N. zibrowii* are much higher and are interpreted to be controlled by  
704 strong vital effects (Wisshak et al., 2008). Contrary to other modern oyster studies (Surge and  
705 Lohmann, 2008; Ullmann et al., 2010; Titschack et al., 2010), Wisshak et al. (2008) do report an  
706 isotopic offset between vesicular and foliated calcite, but  $\delta^{18}\text{O}$  values in vesicular calcite are  
707 reported higher than in foliated calcite, opposite to what was observed in the specimens in this  
708 study (**Figure 5**). A strong ontogenetic trend in  $\delta^{13}\text{C}$  observed in the juvenile part of *N. zibrowii*  
709 records is again opposite to the trend in  $\delta^{13}\text{C}$  observed in this study. This shows that the common  
710 explanation of incorporation of isotopically light  $\text{CO}_2$  into the shell due to enhanced metabolic rate in  
711 the juvenile stage (e.g. Jones et al., 1986; Lorrain et al., 2005; Gillikin et al., 2007; Wisshak et al.,  
712 2008) does not explain the  $\delta^{13}\text{C}$  trend in M6 and M11 shells in this study (**Figure 5**). Instead, any  
713 trends in  $\delta^{13}\text{C}$  in these shells are most likely caused by the effects of sampling and incorporating  
714 recrystallized vesicular calcite into the stable isotope samples, which is also evident from the  
715 elevated Fe concentrations in these shells. The fact that Fe concentrations in M11 are highest in the  
716 ontogenetically oldest part of the record further confirms that the observed drop in stable isotope  
717 values towards the ontogenetically oldest part of this record is caused by diagenesis, and is not an  
718 ontogenetic trend. This is in agreement with work on extant oysters, in which such an ontogenetic





719 trend is generally absent (Surge et al., 2001; Surge and Lohmann, 2008; Ullmann et al., 2010). The  
720 vast difference in geochemical records between these closely related bivalve taxa shows that vital  
721 effects (growth and metabolic rates) play a large role in their mineralization, and that independent  
722 control on the growth rates of these bivalves could be crucial in disentangling internal from external  
723 forcing in bivalve shells. In terms of their expression of proxy records and their environmental niche,  
724 records from *P. vesicularis* shells obtained in this study show much closer resemblance to those of *H.*  
725 *hyotis* and marine *Crassostrea gigas* (Surge and Lohmann, 2008; Ullmann et al., 2010) than to those  
726 of *N. zibrowii*, making *H. hyotis* the best modern analogue to compare with records from shallow  
727 marine *Pycnodonte* shells.

#### 728 6.3.4 Timing of shell deposition and seasonality

729 The  $\delta^{18}\text{O}$  values of the specimens of *H. hyotis* studied by Titschak et al. (2010) are higher than the  
730  $\delta^{18}\text{O}$  values of our specimens of *P. vesicularis*. Presumably, this is because the specimens studied by  
731 Titschak et al. (2010) grew in an environment characterized by a strong evaporative setting (Safaga  
732 Bay). This setting likely resulted in a higher salinity and  $\delta^{18}\text{O}_{\text{seawater}}$  (2.17‰) than in the Neuquén  
733 Basin (-2.8‰ based on clumped isotope results from well-preserved shells in this study). As a  
734 consequence,  $\delta^{18}\text{O}$  records *H. hyotis* in Titschak et al., (2010) are strongly correlated with both Sea  
735 Surface Temperature (SST) and Sea Surface Salinity (SSS). Such an interplay of salinity and  
736 temperature on stable isotope composition of bivalve calcite has been studied in *Crassostrea*  
737 *virginica* that grew under changing salinity conditions (Surge et al., 2001). However, in contrast to  
738 estuarine *C. virginica* studied by Surge et al. (2001), where both stable isotope records are in phase,  
739 the best preserved specimen in our study (M0) presents a (shifted) anti-phase relationship between  
740  $\delta^{18}\text{O}$  and  $\delta^{13}\text{C}$ . Following the rationale that annual lows in  $\delta^{13}\text{C}$  occur in mid-summer in *P. vesicularis*,  
741 this would suggest that the lowest  $\delta^{18}\text{O}$  values are reached in spring (September-November). As  $\delta^{18}\text{O}$   
742 is negatively correlated to temperature and positively correlated to salinity, this would suggest that  
743  $\delta^{18}\text{O}_{\text{shell}}$  variations in our records are more strongly forced by changes in salinity rather than in  
744 temperature, since sea surface temperature is unlikely to be higher in spring than in summer. If so,  
745 our record suggests that the Neuquén basin experienced a decrease in salinity in the spring. Highest  
746 salinities are reached in summer and autumn and lowest salinities in winter to spring, possibly  
747 corresponding to a winter-spring precipitation maximum similar to the present day situation at this  
748 latitude in this region (Servicio Meteorológico Nacional, 2017).

#### 749 6.3.5 Palaeoproductivity

750 The fact that a minimum in Zn/Ca coincides with a maximum in S/Ca and  $\delta^{13}\text{C}$  and a minimum in  $\delta^{18}\text{O}$   
751 in the well preserved M0 specimen (**Figure 5 and 6**) is in agreement with the proposed explanation  
752 of these seasonal records. Zn concentrations in bivalve shells drop during a productivity bloom,  
753 which occurs in the spring season (September-November; Calvert and Pedersen, 1993; Jackson et al.,  
754 1993; Guo et al., 1997, de Winter et al., 2017a). The observation that a minimum in Zn/Ca coincides  
755 with the lowest  $\delta^{18}\text{O}$  values which occurred in spring and precedes the minimum in  $\delta^{13}\text{C}$  that  
756 occurred in mid-summer is consistent with the hypothesis of spring blooms affecting the amount of  
757 bio-available Zn in the surface ocean and forcing Zn/Ca ratios in the shells of *P. vesicularis* (Guo et  
758 al., 2002). This explanation is further supported by the timing of the onset of the drop in Zn/Ca  
759 synchronous with a maximum in  $\delta^{13}\text{C}$ . The annual  $\delta^{13}\text{C}$  cycle in the closely related *H. hyotis* was also  
760 proposed to reflect a seasonality in productivity by Titschak et al. (2010), showing that the drop in  
761 Zn/Ca may indeed be related to a spring bloom in productivity. Increased fresh water input into the  
762 basin during spring, which caused the low salinity conditions that are observed in the  $\delta^{18}\text{O}$  records,  
763 could have provided the nutrients that initiated this productivity bloom. Seasonal decreases in  
764 salinity are in agreement with reconstructions by Woelders et al. (2017).



#### 765 6.3.6 Physiological effects

766 The observed anticorrelation between  $\delta^{18}\text{O}$  and S/Ca in specimen M0 suggests that in *P. vesicularis*,  
767 S/Ca responds as a physiological parameter that co-varies with seasonal changes, such as food  
768 availability, growth or respiration rate. This response has also been inferred for other groups of  
769 bivalves, where S/Ca ratios were considered to reflect metabolic rates (e.g. Rosenberg and Hughes,  
770 1991). A peak in S/Ca during the spring season, when a productivity bloom coincides with a potential  
771 decrease in salinity is in agreement with this explanation. Such environmental perturbations affected  
772 the growth of the bivalve and have been linked to an increase in the incorporation of sulphur into  
773 the organic matrix of the bivalve shell (Lorens and Bender, 1980). The fact that the amplitude of S/Ca  
774 variations in the record of M6 increases in the part of the shell where vesicular calcite penetrates  
775 the shell hinge (**Figure 5**) supports the hypothesis that these disturbances of the shell hinge indicate  
776 periods of physiological stress experienced by the bivalve (Müller, 1970). Interestingly, the year stack  
777 of specimen M0 shows a smaller second peak in Zn/Ca and S/Ca that coincides with autumn if the  
778 interpretation of phase relationships between records is correct. This may reflect a smaller  
779 productivity bloom in autumn. Similarly, a decrease in Sr/Ca ratios synchronous with the peak in  $\delta^{13}\text{C}$   
780 suggests a physiological origin of the seasonality in this proxy. The fact that Sr/Ca ratios are lower  
781 during the low-salinity, high-productivity spring season in which growth was probably slower is in  
782 agreement with relationships between Sr/Ca and growth rate found in modern bivalves (e.g. Lorrain  
783 et al., 2005; Gillikin et al., 2005a). As mentioned above, care must be taken to extrapolate these  
784 interpretations since they are based on only one well-preserved shell.

#### 785 6.4 Temperature proxies

786 An overview of all temperature proxies used in this study is plotted in **Figure 9**. This figure illustrates  
787 some of the complexity of combining these different proxies in *P. vesicularis* to reconstruct  
788 seasonality. Combination of the  $\delta^{18}\text{O}_{\text{sw}}$  values reconstructed using clumped isotope analysis with the  
789 high-resolution  $\delta^{18}\text{O}$  records yields a tentative sub-annual palaeotemperature reconstruction for all  
790 shell records. However, the variations in these records may not reflect true sub-annual temperature  
791 variations, especially since it is likely that salinity in the Neuquén Basin did not remain constant  
792 through the year (see 5.3.4). Temperature reconstructions based on clumped isotope and  $\delta^{18}\text{O}$   
793 records are systematically lower than the  $\text{TEX}_{86}^{\text{H}}$  temperatures. This offset can partially be explained  
794 by the fact that  $\text{TEX}_{86}^{\text{H}}$  is calibrated to sea surface temperatures while *P. vesicularis* lived 50-75 m  
795 below sea level (Scasso et al., 2005), in waters that were likely slightly cooler than those at the sea  
796 surface. However, this difference is most likely not enough to explain the offset of  $\pm 15^\circ\text{C}$  between  
797 clumped isotope and  $\text{TEX}_{86}^{\text{H}}$  temperature reconstructions. Over the past years, several studies have  
798 highlighted the complexity of shallow marine  $\text{TEX}_{86}$  records and have shown that temperature  
799 reconstructions by this method may be biased (e.g. Jia et al. 2017). Similarly, in the compilation  
800 study of O'Brien et al. (2017), Cretaceous  $\text{TEX}_{86}$ -based sea surface temperatures are systematically  
801 higher than planktic foraminiferal  $\delta^{18}\text{O}$ -based temperatures. In some settings,  $\text{TEX}_{86}$  has been shown  
802 to predominantly reflect summer temperatures (Schouten et al., 2013). It is possible that also in the  
803 Neuquén basin  $\text{TEX}_{86}^{\text{H}}$  reconstructed temperatures are biased towards summer-season  
804 temperatures. In contrast, clumped isotope thermometry on our *P. vesicularis* specimens  
805 reconstructs a mean value of the entire growth season of the bivalve. Yet, it is likely that growth in  
806 these bivalves slowed or ceased during the spring and summer season (as is evident from Sr/Ca  
807 ratios, see 5.3.6). The year stack in **Figure 8** also shows that low  $\delta^{18}\text{O}$  values make up a much smaller  
808 portion of the year than the higher  $\delta^{18}\text{O}$  values, suggesting a growth stop in the low- $\delta^{18}\text{O}$  season. It is  
809 therefore likely that temperature reconstructions of both clumped isotope thermometry and  $\text{TEX}_{86}^{\text{H}}$   
810 measurements are seasonally biased and that the mean annual temperature lies in between these



811 two estimates. Alternatively, more vesicular calcite might have been incorporated into the shell  
812 hinge as a result of more stressful growth conditions (Müller, 1970; see 5.2.1) causing these warm  
813 seasons to be selectively overprinted by diagenesis. Indeed, this seems to be the case in the record  
814 of M4, where low values in  $\delta^{18}\text{O}$ , associated with the spring season, are more characterized by  
815 diagenetic alteration than parts of the year (**Figure 9**). If vesicular calcite is avoided in clumped  
816 isotope sampling, this will cause a bias towards colder seasons for clumped isotope temperatures.  
817 However, in practice it will be difficult to avoid these lobes of vesicular calcite and small amounts are  
818 likely to be included in clumped isotope samples, leading to higher palaeotemperature  
819 reconstructions.

820 As mentioned above, several temperature calibrations exist for Mg/Ca ratios in bivalves. The most  
821 likely candidates for temperature reconstruction based on Mg/Ca of *P. vesicularis* are the  
822 calibrations based on ostreid bivalves. Promising examples are the calibrations by Mouchi et al.  
823 (2013, based on juvenile specimens of the pacific oyster *Crassostrea gigas*) and Surge and Lohmann  
824 (2008; based on *Crassostrea virginica*). A factor that complicates the interpretation of Mg/Ca ratios  
825 in terms of temperature is the fact that sea water Mg/Ca ( $\text{Mg}/\text{Ca}_{\text{ocean}}$ ) has changed over geological  
826 timescales, and is thought to have been much lower in the late Maastrichtian than in the present-  
827 day ocean (Maastrichtian  $\text{Mg}/\text{Ca}_{\text{ocean}}$  of 1-2 mol/mol compared to 5 mol/mol in the modern ocean;  
828 Stanley and Hardie, 1998; Coggon et al., 2010). This complicates the use of modern transfer  
829 functions which were established for bivalves growing in modern ocean conditions. Since these  
830 changing ocean compositions have most likely influenced Mg/Ca ratios in calcifying organisms (Lear  
831 et al., 2015), temperature calibrations need to be corrected accordingly (de Winter et al., 2017a).  
832 Therefore, here,  $\text{Mg}/\text{Ca}_{\text{ocean}}$  ratios of  $\sim 1.5$  mol/mol were used to represent average Maastrichtian  
833 ocean water, about 3.3 times lower than in the modern ocean. With this correction, the *C. virginica*  
834 temperature calibration by Surge and Lohmann (2008; **Figure 9**) approach reconstructions based on  
835 the other proxies in terms of temperature seasonality, while the calibration of Mouchi et al. (2013)  
836 seems to significantly overestimate temperature ( $\text{MAT} > 60^\circ\text{C}$ ). Reconstructions based on the Mg/Ca  
837 calibration of Surge and Lohmann (2008) yield sea water temperatures ( $20^\circ\text{C} \pm 10^\circ\text{C}$ ) slightly higher  
838 than those observed in the  $\delta^{18}\text{O}_{\text{sw}}$ -corrected  $\delta^{18}\text{O}$  record.

839 Since Mg/Ca ratios yield temperatures between clumped isotope and  $\text{TEX}_{86}^{\text{H}}$  reconstructions, it is  
840 tentative to assume that they more closely represent mean annual temperatures than the other  
841 proxies. However, there are large differences ( $>10^\circ\text{C}$ ) between temperature reconstructions of  
842 Mg/Ca and  $\delta^{18}\text{O}$  in some parts of the records. Furthermore, the well-preserved M0 shell record  
843 shows an anticorrelation between the seasonal fluctuations of the two temperature records in parts  
844 of the record, suggesting that at least one of the proxies may largely be controlled by a factor other  
845 than ambient temperature (although phasing arguments may be affected by the relative scaling of  
846 trace element and stable isotope records). Seasonal changes in salinity cannot account for this  
847 difference between the proxies, as a seasonal increase in salinity of approximately 20 PSU would be  
848 required to account for the offset in temperature between the proxies (Ravelo and Hillaire-Marcel,  
849 2007). Such a severe change in salinity is not consistent with earlier palaeoenvironmental  
850 reconstructions in the Neuquén Basin (Prámparo et al. 1996; Prámparo and Papú 2006; Woelders et  
851 al. 2017). Additionally, there seems to be no a priori reason why Mg/Ca temperature calibration of  
852 Surge and Lohmann (2008) would be the most suitable calibration for *P. vesicularis*, which may  
853 require its own species-specific calibration. If seasonal growth cessations are present in *P.*  
854 *vesicularis*, they would affect Mg/Ca as well as  $\delta^{18}\text{O}$  and cause Mg/Ca records to have the same  
855 seasonal bias. It must be noted that the fact that trace element records and stable isotope records  
856 were measured using different methods makes it possible that the records are slightly shifted with  
857 respect to each other (see section 4.5). As a consequence, phase relationships between Mg/Ca and



858  $\delta^{18}\text{O}$  temperature reconstructions may have been distorted. Closer observation of **Figure 9** indeed  
859 shows that temperature reconstructions based on these two records are in some cases shifted with  
860 respect to each other. This might explain part of the offset between the reconstructions and render  
861 Mg/Ca temperatures more probable. Nevertheless, the uncertainties of Mg/Ca temperature  
862 reconstructions in bivalves, together with the observed lack of temperature dependence of Mg/Ca  
863 ratios in the closely related *Pycnodonte zibrowii*, leads to the conclusion that temperature  
864 reconstructions based on Mg/Ca ratios in *Pycnodonte* oysters are difficult.

865 In summary,  $\delta^{18}\text{O}$  values in the shells of *P. vesicularis* have been shown to vary with changes in  
866 salinity in this setting. Temperatures reconstructed by clumped isotope thermometry from well-  
867 preserved parts of different bivalve shells agree and seem to be the most reliable method for  
868 temperature reconstruction. These clumped isotope temperature reconstructions are in agreement  
869 with present-day average annual temperatures in the region ( $\sim 10\text{--}15^\circ\text{C}$ ; Servicio Meteorológico  
870 Nacional, 2017), while they are slightly below model and proxy-based SST reconstructions for the  
871 Maastrichtian mid-latitudes ( $20\text{--}25^\circ\text{C}$ ; e.g. [Donnadieu et al., 2006](#); [Brugger et al., 2017](#); [O'Brien et al., 2017](#)).  
872 Comparison of all palaeotemperature proxies in this study shows that  $\text{TEX}_{86}^{\text{H}}$  temperature  
873 reconstructions ( $27\text{--}30^\circ\text{C}$ ) likely overestimate MAT, while clumped isotope thermometry might  
874 underestimate it. Mg/Ca temperature reconstructions show promising results ( $15\text{--}20^\circ\text{C}$ ), but depend  
875 heavily on the calibration that is used and are therefore considered problematic. The best approach  
876 to reconstruct palaeotemperature seasonality from *Pycnodonte* shells would be to microsample the  
877 foliated calcite of the shells for clumped isotope analysis. This microsampling can be guided by  
878 records of conventional stable isotope ratios and trace element concentrations to ensure the  
879 sampling of material from different seasons. Via this approach, both seasonality in temperature and  
880 salinity can be reconstructed from *Pycnodonte* shells, and the effects of salinity and temperature on  
881  $\delta^{18}\text{O}$  values can be disentangled.

## 882 7. Conclusions and recommendations

883 This study represents a first attempt to employ the shells of the honeycomb oyster *Pycnodonte*  
884 *vesicularis* for the reconstruction of late Maastrichtian palaeoseasonality. The multi-proxy approach  
885 applied in this work demonstrates the complexity of such attempts to reconstruct  
886 palaeoenvironmental conditions. Yet, this approach also demonstrates the value of using a range of  
887 different methods to characterize the preservation state and chemical composition of fossil bivalve  
888 calcite. Based on the results presented in this work, several recommendations can be made for the  
889 use of shells from *P. vesicularis* for the reconstruction of palaeoseasonality and palaeoenvironment.  
890 Detailed analysis of shell structure and preservation shows that shells of *P. vesicularis*, like other  
891 species of the Order Ostreoida, are characterized by two major micromorphologies of calcite, which  
892 were referred to by Carriker et al. (1980b) as “chalky” and “foliated” calcite. In the case of *P.*  
893 *vesicularis*, CT scanning shows that these “chalky” (vesicular) calcite layers are characterized by a  
894 high degree of porosity (up to 65%) and are therefore very permeable for pore fluids (**Figure 4**). The  
895 thin walls of the vesicular calcite structure provide a lot of surface contact between permeating pore  
896 fluid and the calcite, making it prone to recrystallization (**Figure 3**). The recrystallization and the  
897 precipitation of secondary carbonates in this porous micromorphology therefore renders the  
898 vesicular calcite of pycnodontin bivalves poorly suitable for palaeoenvironmental reconstruction. In  
899 addition, pore fluid can enter the shells of *P. vesicularis* post mortem through bore holes, for  
900 example made by polychaete worms. Subsequently, recrystallization and precipitation of secondary  
901 carbonates in equilibrium with these reducing pore fluids raises the concentrations of Mn and Fe  
902 (see XRF mapping and CL images in **Figure 3**) and lowers stable isotope ratios. Hence, when selecting  
903 specimens of *P. vesicularis* for palaeoseasonality reconstructions, specimens affected by boring



904 organisms are best avoided or treated with care. Micro-analytical techniques such as  
905 cathodoluminescence microscopy, optical microscopy and  $\mu$ XRF mapping allows to avoid these  
906 zones of recrystallization.

907 Foliated calcite layers in the shell hinge of *P. vesicularis* are less affected by these diagenetic  
908 processes and stable isotope, clumped isotope and trace element compositions of these layers  
909 suggest preservation of primary calcite, making it suitable for palaeoseasonality reconstruction.  
910 However, care must be taken in sampling these parts of the shells of *P. vesicularis*, as lobes of  
911 vesicular calcite can extend into the hinge of the shells. Such lobes of vesicular calcite can be very  
912 thin, and can be difficult to avoid while microsampling for stable isotope ratios. Incorporation of  
913 vesicular calcite into stable isotope samples will significantly alter the measured stable isotope ratios  
914 and influence the interpretation of palaeoseasonality. Clumped isotope analysis of samples  
915 containing this vesicular calcite yield much higher temperatures than samples of foliated calcite,  
916 suggesting diagenetic overprinting of the stable isotope signal. The multi-proxy approach in this  
917 study allows the distinction of diagenetic parts in fossil bivalve shells and aids in the evasion of  
918 diagenetically altered parts of the shells and the consideration of only well-preserved parts.

919 Future work on *P. vesicularis* shells, as well as other gryphaeid shells that contain multiple  
920 microstructures, aiming at the reconstruction of palaeoseasonality over geological time scales  
921 should benefit from the application of a multi-proxy approach that allows the interpretation of  
922 seasonally changing environmental parameters. However, the establishment of a shell chronology  
923 from these records can be difficult, as selective diagenetic overprinting, the occurrence of growth  
924 cessations and the complexity of synchronizing proxy records from multiple methods can complicate  
925 the interpretation of phase relationships between proxies. Multi-proxy analysis on one exceptionally  
926 well-preserved specimen demonstrates how the timing of seasonal deposition of the shell could be  
927 determined from the phase relationships between proxies. If applied correctly, this approach also  
928 allows the separation of the effects of, for example, temperature and salinity on the stable isotope  
929 ratios in the shells. However, it must be noted that extrapolation of results from one well-preserved  
930 specimen means that the interpretation of phase relationships in this study must remain tentative.  
931 Even though the establishment of shell chronology for less well-preserved samples is difficult, multi-  
932 proxy records from well-preserved parts of these shells can still yield information about the sub-  
933 annual variation of proxies in *P. vesicularis*. Comparison of these multi-proxy shell records with  
934 contextual proxy reconstructions allows palaeoseasonality reconstructions to be placed in a larger  
935 geological context and allows the discussion of different palaeotemperature proxies.

936 Records of uncontaminated foliated calcite in the hinge of well-preserved specimens of *P. vesicularis*  
937 yield a mean annual sea water temperature in the late Maastrichtian Neuquén Basin of 11°C, which  
938 is lower than reconstructions based on contextual  $\text{TEX}_{86}^{\text{H}}$  palaeothermometry ( $\pm 27^\circ\text{C}$ ). This  
939 comparison suggests that the  $\text{TEX}_{86}^{\text{H}}$  method overestimates mean annual temperatures in this  
940 setting, possibly representing summer surface water temperatures. Clumped isotope thermometry  
941 of bulk foliated calcite samples likely underestimates the annual mean because the warm spring and  
942 early summer season is underrepresented in the shells due to slower growth or growth cessations. A  
943 seasonality in  $\delta^{18}\text{O}$  of about 1‰ is ascribed to a combination of decreased salinity by fresh water  
944 input in the spring season and a moderate temperature seasonality, but the aforementioned  
945 seasonal bias prevents capture of the full seasonal cycle in this record. Attempts to verify the  
946 seasonality in SST by Mg/Ca ratios of shell calcite are complicated by uncertainties about vital effects  
947 on the incorporation of Mg into the bivalve shell. After correction for lower sea water Mg/Ca ratios  
948 in the Late Cretaceous, Mg/Ca temperatures calculated using the oyster-based calibration of Surge  
949 and Lohmann (2008) fall between temperatures of clumped isotope palaeothermometry and those



950 of  $\text{TEX}_{86}^{\text{H}}$  palaeothermometry and reveal a pattern similar to the  $\delta^{18}\text{O}$  records. While it is tentative to  
 951 conclude that this record most closely reconstructs the temperature seasonality, the uncertainties  
 952 involved in bivalve Mg/Ca records precludes such a straightforward conclusion.

953 This multi-proxy work shows that, even using several independent palaeotemperature  
 954 reconstruction methods, the reconstruction of temperature seasonality from fossil bivalve calcite is  
 955 strongly complicated by the influence of other palaeoenvironmental parameters that affect the  
 956 chemistry of bivalve shells. Yet, the successful application of clumped isotope thermometry on fossil  
 957 bivalve calcite in this study indicates that temperature seasonality in fossil ostreid bivalves may be  
 958 constrained by the sequential analysis of foliated calcite samples using this method.

959

#### 960 Acknowledgements

961 Niels J. de Winter is financed by a personal PhD fellowship from IWT Flanders (IWT700). This  
 962 research was partly financed by the FOD40 Chicxulub grant obtained by Philippe Claeys. Robert P.  
 963 Speijer is funded by the Research Foundation Flanders (FWO grant G.0B85.13). Johan Vellekoop is  
 964 also funded by a personal research grant from FWO (grant 12Z6618N). Thanks go to the Hercules  
 965 foundation Flanders for acquisition of XRF instrumentation (grant HERC1309) and VUB Strategic  
 966 Research Program for support of the AMGC research group. The authors thank Prof. Rudy Swennen  
 967 from the KU Leuven for analytical support. The author declares that there are no conflicts of  
 968 interest.

969

#### 970 References

- 971 Abele, D., Brey, T., Philipp, E., 2009. Bivalve models of aging and the determination of molluscan lifespans. *Experimental gerontology* 44,  
 972 307–315.
- 973 Al-Aasm, I.S., Veizer, J., 1986. Diagenetic stabilization of aragonite and low-Mg calcite, I. Trace elements in rudists. *Journal of*  
 974 *Sedimentary Research* 56.
- 975 Andrews, J.E., Tandon, S.K., Dennis, P.F., 1995. Concentration of carbon dioxide in the Late Cretaceous atmosphere. *Journal of the*  
 976 *Geological Society* 152, 1–3.
- 977 Ayyasami, K., 2006. Role of oysters in biostratigraphy: A case study from the Cretaceous of the Ariyalur area, southern India. *Geosciences*  
 978 *Journal* 10, 237–247.
- 979 Baldoni, A.M., 1992. Palynology of the lower lefipan formation (upper cretaceous) of barranca de los perros, chubut province, Argentina.  
 980 part I. Cryptogam spores and gymnosperm pollen. *Palynology* 16, 117–136.
- 981 Barbin, V., 2000. Cathodoluminescence of carbonate shells: biochemical vs diagenetic process, in: *Cathodoluminescence in Geosciences*.  
 982 Springer, pp. 303–329.
- 983 Barreda, V., Palazzesi, L., 2007. Patagonian vegetation turnovers during the Paleogene-early Neogene: origin of arid-adapted floras. *The*  
 984 *botanical review* 73, 31–50.
- 985 Barreda, V.D., Cúneo, N.R., Wilf, P., Currano, E.D., Scasso, R.A., Brinkhuis, H., 2012. Cretaceous/Paleogene floral turnover in Patagonia:  
 986 drop in diversity, low extinction, and a Classopollis spike. *PLoS One* 7, e52455.
- 987 Berner, R., 1990. Atmospheric carbon dioxide levels over Phanerozoic time. *Science* 249, 1382–1386.
- 988 Bertels, A., 2013. Micropaleontología y estratigrafía del límite Cretácico-Terciario en Huantrai-co (provincia de Neuquén). *Ostracoda. Parte*  
 989 *1: Cytherellidae, Bairdiidae, Pontocypridinae, Buntoniinae y Trachyleberidinae (pro parte)*. *Ameghiniana* 5, 279–298.
- 990 Bieler, R., Mikkelsen, P.M., Lee, T., Foighil, D.Ó., 2004. Discovery of the Indo-Pacific oyster *Hyothis hyotis* (Linnaeus, 1758) in the  
 991 Florida Keys (Bivalvia: Gryphaeidae). *Molluscan Research* 24, 149–159.
- 992 Brand, U., Veizer, J., 1981. Chemical diagenesis of a multicomponent carbonate system-2: stable isotopes. *Journal of Sedimentary Research*  
 993 51.
- 994 Brand, U., Veizer, J., 1980. Chemical diagenesis of a multicomponent carbonate system-1: Trace elements. *Journal of Sedimentary*  
 995 *Research* 50.
- 996 Brezina, S.S., Romero, M.V., Casadío, S., Bremec, C., 2014. Boring Polychaetes Associated with Pycnodonte (Phygraea) Vesicularis  
 997 (Lamarck) from the Upper Cretaceous of Patagonia. A Case of Commensalism? *Ameghiniana* 51, 129–140.
- 998 Brugger, J., Feulner, G., Petri, S., 2017. Baby, it's cold outside: Climate model simulations of the effects of the asteroid impact at the end of  
 999 the Cretaceous: Chicxulub impact cooling. *Geophysical Research Letters* 44, 419–427. doi:10.1002/2016GL072241
- 1000 Calvert, S.E., Pedersen, T.F., 1993. Geochemistry of Recent oxic and anoxic marine sediments: Implications for the geological record.  
 1001 *Marine Geology, Marine Sediments, Burial, Pore Water Chemistry, Microbiology and Diagenesis* 113, 67–88. doi:10.1016/0025-  
 1002 3227(93)90150-T
- 1003 Carré, M., Bentalab, I., Blamart, D., Ogle, N., Cardenas, F., Zevallos, S., Kalin, R.M., Ortlieb, L., Fontugne, M., 2005. Stable isotopes and  
 1004 sclerochronology of the bivalve *Mesodesma donacium*: potential application to Peruvian paleoceanographic reconstructions.  
 1005 *Palaeogeography, Palaeoclimatology, Palaeoecology* 228, 4–25.
- 1006 Carriker, Melbourne R., Palmer, R.E., Sick, L.V., Johnson, C.C., 1980a. Interaction of mineral elements in sea water and shell of oysters



- 1007 (Crassostrea virginica (Gmelin)) cultured in controlled and natural systems. *Journal of experimental marine biology and ecology*  
 1008 46, 279–296.
- 1009 Carriker, M.R., Palmer, R.E., Prezant, R.S., 1980b. Ultrastructural morphogenesis of prodissoconch and early dissoconch valves of the  
 1010 oyster *Crassostrea virginica*. College of Marine Studies, University of Delaware.
- 1011 Chauvaud, L., Lorrain, A., Dunbar, R.B., Paulet, Y.-M., Thouzeau, G., Jean, F., Guarini, J.-M., Mucciarone, D., 2005. Shell of the Great  
 1012 Scallop *Pecten maximus* as a high-frequency archive of paleoenvironmental changes. *Geochemistry, Geophysics, Geosystems* 6.  
 1013 Chinzei, K., Seilacher, A., 1993. Remote Biomineralization I: Fill skeletons in vesicular oyster shells. (With 7 figures in the text). *Neues*  
 1014 *Jahrbuch für Geologie und Palaontologie-Abhandlungen* 190, 349–362.
- 1015 Cleroux, C., Cortijo, E., Anand, P., Labeyrie, L., Bassinot, F., Caillon, N., Duplessy, J.-C., 2008. Mg/Ca and Sr/Ca ratios in planktonic  
 1016 foraminifera: Proxies for upper water column temperature reconstruction. *Paleoceanography* 23.
- 1017 Coggon, R.M., Teagle, D.A., Smith-Duque, C.E., Alt, J.C., Cooper, M.J., 2010. Reconstructing past seawater Mg/Ca and Sr/Ca from mid-  
 1018 ocean ridge flank calcium carbonate veins. *Science* 327, 1114–1117.
- 1019 Dale, A., John, C.M., Mozley, P.S., Smalley, P.C., Mugeridge, A.H., 2014. Time-capsule concretions: unlocking burial diagenetic  
 1020 processes in the Mancos Shale using carbonate clumped isotopes. *Earth and Planetary Science Letters* 394, 30–37.
- 1021 de Winter, N.J., Zeeden, C., Hilgen, F.J., 2014. Low-latitude climate variability in the Heinrich frequency band of the Late Cretaceous  
 1022 greenhouse world. *Climate of the Past* 10, 1001–1015. doi:10.5194/cp-10-1001-2014.
- 1023 de Winter, N.J., Claeys, P., 2016. Micro X-ray fluorescence ( $\mu$ XRF) line scanning on Cretaceous rudist bivalves: A new method for  
 1024 reproducible trace element profiles in bivalve calcite. *Sedimentology*. doi:10.1111/sed.12299
- 1025 de Winter, N.J., Goderis, S., Dehairs, F., Jagt, J.W.M., Fraaije, R.H.B., Van Malderen, S.J.M., Vanhaecke, F., Claeys, P., 2017a Tropical  
 1026 seasonality in the late Campanian (Late Cretaceous): Comparison between multiproxy records from three bivalve taxa from  
 1027 Oman. *Palaeogeography, Palaeoclimatology, Palaeoecology*, <https://doi.org/10.1016/j.palaeo.2017.07.031>.
- 1028 de Winter, N.J., Sinnesael, M., Makarona, C., Vansteenberge, S., Claeys, P., 2017b. Trace element analyses of carbonates using portable and  
 1029 micro-X-ray fluorescence: Performance and optimization of measurement parameters and strategies. *Journal of Analytical*  
 1030 *Atomic Spectrometry*.
- 1031 Defliese, W.F., Hren, M.T., Lohmann, K.C., 2015. Compositional and temperature effects of phosphoric acid fractionation on  $\Delta 47$  analysis  
 1032 and implications for discrepant calibrations. *Chemical Geology* 396, 51–60.
- 1033 Dennis, K.J., Affek, H.P., Passey, B.H., Schrag, D.P., Eiler, J.M., 2011. Defining an absolute reference frame for “clumped” isotope studies  
 1034 of CO<sub>2</sub>. *Geochimica et Cosmochimica Acta* 75, 7117–7131.
- 1035 Dettman, D.L., Kohn, M.J., Quade, J., Ryerson, F.J., Ojha, T.P., Hamidullah, S., 2001. Seasonal stable isotope evidence for a strong Asian  
 1036 monsoon throughout the past 10.7 my. *Geology* 29, 31–34.
- 1037 Dettman, D.L., Lohmann, K.C., 2000. Oxygen isotope evidence for high-altitude snow in the Laramide Rocky Mountains of North America  
 1038 during the Late Cretaceous and Paleogene. *Geology* 28, 243–246. doi:10.1130/0091-7613(2000)28<243:OIEFHS>2.0.CO;2
- 1039 Dettman, D.L., Lohmann, K.C., 1993. Seasonal Change in Paleogene Surface Water  $\delta 18O$ : Fresh-Water Bivalves of Western North  
 1040 America. *Climate change in continental isotopic records* 153–163.
- 1041 Dlugokencky, E., Tans, P., 2017. NOAA/ESRL ([www.esrl.noaa.gov/gmd/ccgg/trends/](http://www.esrl.noaa.gov/gmd/ccgg/trends/)), accessed 31/01/2017.
- 1042 Dodd, J.R., Crisp, E.L., 1982. Non-linear variation with salinity of Sr/Ca and Mg/Ca ratios in water and aragonitic bivalve shells and  
 1043 implications for paleosalinity studies. *Palaeogeography, Palaeoclimatology, Palaeoecology* 38, 45–56.
- 1044 Donnadiou, Y., Pierrehumbert, R., Jacob, R., Fluteau, F., 2006. Modelling the primary control of paleogeography on Cretaceous climate.  
 1045 *Earth and Planetary Science Letters* 248, 426–437. doi:10.1016/j.epsl.2006.06.007
- 1046 Dreier, A., Loh, W., Blumenberg, M., Thiel, V., Hause-Reitner, D., Hoppert, M., 2014. The isotopic biosignatures of photo-vs. thiotrophic  
 1047 bivalves: are they preserved in fossil shells? *Geobiology* 12, 406–423.
- 1048 Duinker, J.C., Nolting, R.F., Michel, D., 1982. Effects of salinity, pH and redox conditions on the behaviour of Cd, Zn, Ni and Mn in the  
 1049 Scheldt estuary. *Thalassia Jugosl* 18, 191–202.
- 1050 Dunbar, R.B., Wefer, G., 1984. Stable isotope fractionation in benthic foraminifera from the Peruvian continental margin. *Marine Geology*  
 1051 59, 215–225.
- 1052 Ekart, D.D., Cerling, T.E., Montanez, I.P., Tabor, N.J., 1999. A 400 million year carbon isotope record of pedogenic carbonate: implications  
 1053 for paleoatmospheric carbon dioxide. *American Journal of Science* 299, 805–827.
- 1054 Elliot, M., Welsh, K., Chilcott, C., McCulloch, M., Chappell, J., Ayling, B., 2009. Profiles of trace elements and stable isotopes derived  
 1055 from giant long-lived *Tridacna gigas* bivalves: potential applications in paleoclimate studies. *Palaeogeography,*  
 1056 *Palaeoclimatology, Palaeoecology* 280, 132–142.
- 1057 Folk, R.L., Land, L.S., 1975. Mg/Ca ratio and salinity: two controls over crystallization of dolomite. *AAPG bulletin* 59, 60–68.  
 1058 [Fossilworks.org](http://Fossilworks.org): Pycnodonte genus, age range and distribution. Retrieved 14-02-2017
- 1059 Freitas, P., Clarke, L.J., Kennedy, H., Richardson, C., Abrantes, F., 2005. Mg/Ca, Sr/Ca, and stable-isotope ( $\delta^{18}O$  and  $\delta^{13}C$ ) ratio profiles  
 1060 from the fan mussel *Pinna nobilis*: Seasonal records and temperature relationships: *PINNA NOBILIS RATIO PROFILES*.  
 1061 *Geochemistry, Geophysics, Geosystems* 6, n/a-n/a. doi:10.1029/2004GC000872
- 1062 Freitas, P.S., Clarke, L.J., Kennedy, H., Richardson, C.A., Abrantes, F., 2006. Environmental and biological controls on elemental (Mg/Ca,  
 1063 Sr/Ca and Mn/Ca) ratios in shells of the king scallop *Pecten maximus*. *Geochimica et Cosmochimica Acta* 70, 5119–5133.  
 1064 doi:10.1016/j.gca.2006.07.029
- 1065 Freitas, P.S., Clarke, L.J., Kennedy, H.A., Richardson, C.A., 2008. Inter- and intra-specimen variability masks reliable temperature control  
 1066 on shell Mg/Ca ratios in laboratory and field cultured *Mytilus edulis* and *Pecten maximus* (bivalvia). *Biogeosciences Discussions*  
 1067 5, 531–572.
- 1068 Friedman, I., O'NEIL, J., CEBULA, G., 1982. Two New Carbonate Stable-Isotope Standards. *Geostandards Newsletter* 6, 11–12.
- 1069 Friedrich, O., Norris, R.D., Erbacher, J., 2012. Evolution of middle to Late Cretaceous oceans—a 55 my record of Earth's temperature and  
 1070 carbon cycle. *Geology* 40, 107–110.
- 1071 Geist, J., Auerswald, K., Boom, A., 2005. Stable carbon isotopes in freshwater mussel shells: Environmental record or marker for metabolic  
 1072 activity? *Geochimica et Cosmochimica Acta* 69, 3545–3554.
- 1073 Gillikin, D.P., De Ridder, F., Ulens, H., Elskens, M., Keppens, E., Baeyens, W., Dehairs, F., 2005a. Assessing the reproducibility and  
 1074 reliability of estuarine bivalve shells (*Saxidomus giganteus*) for sea surface temperature reconstruction: implications for  
 1075 paleoclimate studies. *Palaeogeography, Palaeoclimatology, Palaeoecology* 228, 70–85.
- 1076 Gillikin, D.P., Lorrain, A., Meng, L., Dehairs, F., 2007. A large metabolic carbon contribution to the  $\delta^{13}C$  record in marine aragonitic  
 1077 bivalve shells. *Geochimica et Cosmochimica Acta* 71, 2936–2946.
- 1078 Gillikin, D.P., Lorrain, A., Navez, J., Taylor, J.W., André, L., Keppens, E., Baeyens, W., Dehairs, F., 2005b. Strong biological controls on  
 1079 Sr/Ca ratios in aragonitic marine bivalve shells. *Geochemistry, Geophysics, Geosystems* 6.
- 1080 Gillikin, D.P., Lorrain, A., Paulet, Y.-M., André, L., Dehairs, F., 2008. Synchronous barium peaks in high-resolution profiles of calcite and  
 1081 aragonite marine bivalve shells. *Geo-Marine Letters* 28, 351–358.



- 1082 Goodwin, D.H., Flessa, K.W., Schöne, B.R., Dettman, D.L., 2001. Cross-calibration of daily growth increments, stable isotope variation,  
 1083 and temperature in the Gulf of California bivalve mollusk *Chione cortezi*: implications for paleoenvironmental analysis. *Palaios*  
 1084 16, 387–398.
- 1085 Grossman, E.L., Ku, T.-L., 1986. Oxygen and carbon isotope fractionation in biogenic aragonite: temperature effects. *Chemical Geology: Isotope Geoscience section* 59, 59–74.
- 1086 Guo, T., DeLaune, R.D., Patrick, W.H., 1997. The influence of sediment redox chemistry on chemically active forms of arsenic, cadmium,  
 1087 chromium, and zinc in estuarine sediment. *Environment International* 23, 305–316.
- 1088 Gutiérrez-Zugasti, I., Clarke, L.J., García-Escárcaga, A., Suárez-Revilla, R., G.N., González-Morales, M. Changes in seawater temperatures  
 1089 in northern Iberia during the Late Pleistocene and Early Holocene. 22<sup>nd</sup> Annual Meeting of the EAA 2016, TH5-13, Abstract 4,  
 1090 September 3, 2016.
- 1091 Habermann, D., 2002. Quantitative cathodoluminescence (CL) spectroscopy of minerals: possibilities and limitations. *Mineralogy and Petrology* 76, 247–259.
- 1092 Hallmann, N., Burchell, M., Brewster, N., Martindale, A., Schöne, B.R., 2013. Holocene climate and seasonality of shell collection at the  
 1093 Dundas Islands Group, northern British Columbia, Canada—A bivalve sclerochronological approach. *Palaeogeography, Palaeoclimatology, Palaeoecology* 373, 163–172.
- 1094 Harzhauser, M., Piller, W.E., Müllgger, S., Grunert, P., Micheels, A., 2011. Changing seasonality patterns in Central Europe from Miocene  
 1095 Climate Optimum to Miocene Climate Transition deduced from the *Crassostrea* isotope archive. *Global and Planetary Change*  
 1096 76, 77–84.
- 1097 Hay, W.W., 2008. Evolving ideas about the Cretaceous climate and ocean circulation. *Cretaceous Research* 29, 725–753.
- 1098 Hayami, I., Kase, T., 1992. A new cryptic species of *Pycnodonte* from Ryukyu Islands: a living fossil oyster. *Nihon Koseibutsu Gakkai hokoku, kiji* 1070–1089.
- 1099 Huber, B.T., Norris, R.D., MacLeod, K.G., 2002. Deep-sea paleotemperature record of extreme warmth during the Cretaceous. *Geology* 30, 123–126. doi:10.1130/0091-7613(2002)030<0123:DSPROE>2.0.CO;2
- 1100 Hunter, S.J., Valdes, P.J., Haywood, A.M., Markwick, P.J., 2008. Modelling Maastrichtian climate: investigating the role of geography,  
 1101 atmospheric CO<sub>2</sub> and vegetation. *Climate of the Past Discussions* 4, 981–1019.
- 1102 Huntington, K.W., Budd, D.A., Wernicke, B.P., Eiler, J.M., 2011. Use of clumped-isotope thermometry to constrain the crystallization  
 1103 temperature of diagenetic calcite. *Journal of Sedimentary Research* 81, 656–669.
- 1104 Iglesias, A., Wilf, P., Johnson, K.R., Zamuner, A.B., Cúneo, N.R., Matheos, S.D., Singer, B.S., 2007. A Paleocene lowland macroflora from  
 1105 Patagonia reveals significantly greater richness than North American analogs. *Geology* 35, 947–950.
- 1106 IPCC, 2014: Climate Change 2014: Synthesis Report. Contribution of Working Groups I, II and III to the Fifth Assessment Report of the  
 1107 Intergovernmental Panel on Climate Change [Core Writing Team, R.K. Pachauri and L.A. Meyer (eds.)]. IPCC, Geneva, Switzerland, 151 pp.
- 1108 Jackson, L.J., Kalf, J., Rasnussen, J.B., 1993. Sediment pH and redox potential affect the bioavailability of Al, Cu, Fe, Mn, and Zn to  
 1109 rooted aquatic macrophytes. *Canadian Journal of Fisheries and Aquatic Sciences* 50, 143–148.
- 1110 Jia, G., X. Wang, W. Guo, and L. Dong (2017), Seasonal distribution of archaeological lipids in surface water and its constraint on their sources  
 1111 and the TEX86 temperature proxy in sediments of the South China Sea. *J. Geophys. Res. Biogeosci.*, 122,  
 1112 doi:10.1002/2016JG003732.
- 1113 Jones, D.S., 1980. Annual cycle of shell growth increment formation in two continental shelf bivalves and its paleoecologic significance. *Paleobiology* 6, 331–340.
- 1114 Jones, D.S., 1983. Sclerochronology: reading the record of the molluscan shell: annual growth increments in the shells of bivalve molluscs  
 1115 record marine climatic changes and reveal surprising longevity. *American Scientist* 71, 384–391.
- 1116 Jones, D.S., Williams, D.F., Romanek, C.S., 1986. Life history of symbiont-bearing giant clams from stable isotope profiles. *Science* 231, 46–49.
- 1117 Kiessling, W., Aragón, E., Scasso, R., Aberhan, M., Kriwet, J., Medina, F., Fracchia, D., 2005. Massive corals in Paleocene siliclastic  
 1118 sediments of Chubut (Argentina). *Facies* 51, 233–241.
- 1119 Kim, S.-T., O’Neil, J.R., 1997. Equilibrium and nonequilibrium oxygen isotope effects in synthetic carbonates. *Geochimica et Cosmochimica Acta* 61, 3461–3475.
- 1120 Kirby, M.X., 2000. Paleocological differences between Tertiary and Quaternary *Crassostrea* oysters, as revealed by stable isotope  
 1121 sclerochronology. *Palaios* 15, 132–141.
- 1122 Kirby, M.X., Soniat, T.M., Spero, H.J., 1998. Stable isotope sclerochronology of Pleistocene and Recent oyster shells (*Crassostrea virginica*). *Palaios* 13, 560–569.
- 1123 Klein, R.T., Lohmann, K.C., Thayer, C.W., 1996a. Bivalve skeletons record sea-surface temperature and  $\delta^{18}\text{O}$  via Mg/Ca and  $^{18}\text{O}/^{16}\text{O}$   
 1124 ratios. *Geology* 24, 415–418.
- 1125 Klein, R.T., Lohmann, K.C., Thayer, C.W., 1996b. Sr/Ca and  $^{13}\text{C}/^{12}\text{C}$  ratios in skeletal calcite of *Mytilus trossulus*: Covariation with  
 1126 metabolic rate, salinity, and carbon isotopic composition of seawater. *Geochimica et Cosmochimica Acta* 60, 4207–4221.
- 1127 Langlet, D., Alunno-Bruscia, M., Raféls, M., Renard, M., Roux, M., Schein, E., Buestel, D., 2006. Experimental and natural  
 1128 cathodoluminescence in the shell of *Crassostrea gigas* from Thau lagoon (France): ecological and environmental implications. *Marine Ecology Progress Series* 317, 143–156.
- 1129 Lartaud, F., De Raféls, M., Ropert, M., Emmanuel, L., Geairon, P., Renard, M., 2010a. Mn labelling of living oysters: artificial and natural  
 1130 cathodoluminescence analyses as a tool for age and growth rate determination of *C. gigas* (Thunberg, 1793) shells. *Aquaculture*  
 1131 300, 206–217.
- 1132 Lartaud, F., Emmanuel, L., De Raféls, M., Pouvreau, S., Renard, M., 2010b. Influence of food supply on the  $\delta^{13}\text{C}$  signature of mollusc  
 1133 shells: implications for palaeoenvironmental reconstructions. *Geo-Marine Letters* 30, 23–34.
- 1134 Lazareth, C.E., Vander Putten, E., André, L., Dehairs, F., 2003. High-resolution trace element profiles in shells of the mangrove bivalve  
 1135 *Isognomon ephippium*: a record of environmental spatio-temporal variations? *Estuarine, Coastal and Shelf Science* 57, 1103–1114.
- 1136 Lear, C.H., Elderfield, H., Wilson, P.A., 2000. Cenozoic deep-sea temperatures and global ice volumes from Mg/Ca in benthic foraminiferal  
 1137 calcite. *Science* 287, 269–272.
- 1138 Lear, C.H., Coxall, H.K., Foster, G.L., Lunt, D.J., Mawbey, E.M., Rosenthal, Y., Sosdian, S.M., Thomas, E., Wilson, P.A., 2015. Neogene  
 1139 ice volume and ocean temperatures: Insights from infaunal foraminiferal Mg/Ca paleothermometry. *Paleoceanography* 30, 1437–1454.
- 1140 Lécuyer, C., Reynard, B., Martineau, F., 2004. Stable isotope fractionation between mollusc shells and marine waters from Martinique  
 1141 Island. *Chemical Geology* 213, 293–305.
- 1142 Linnaeus, Carolus, *Systema naturae per regna tria naturae: secundum classes, ordines, genera, species, cum characteribus, differentiis, synonymis, locis.*, 10th edition, Lars Salvi, Stockholm, 1758
- 1143  
1144  
1145  
1146  
1147  
1148  
1149  
1150  
1151  
1152  
1153  
1154  
1155  
1156





- 1157 Lorens, R.B., Bender, M.L., 1980. The impact of solution chemistry on *Mytilus edulis* calcite and aragonite. *Geochimica et Cosmochimica*  
1158 *Acta* 44, 1265–1278.
- 1159 Lorrain, A., Gillikin, D.P., Paulet, Y.-M., Chauvaud, L., Le Mercier, A., Navez, J., André, L., 2005. Strong kinetic effects on Sr/Ca ratios in  
1160 the calcitic bivalve *Pecten maximus*. *Geology* 33, 965–968.
- 1161 Lorrain, A., Paulet, Y.-M., Chauvaud, L., Dunbar, R., Mucciarone, D., Fontugne, M., 2004.  $\delta^{13}\text{C}$  variation in scallop shells: increasing  
1162 metabolic carbon contribution with body size? *Geochimica et Cosmochimica Acta* 68, 3509–3519.
- 1163 Loyd, S.J., Corsetti, F.A., Eiler, J.M., Tripathi, A.K., 2012. Determining the diagenetic conditions of concretion formation: assessing  
1164 temperatures and pore waters using clumped isotopes. *Journal of Sedimentary Research* 82, 1006–1016.
- 1165 Machel, H.G., Burton, E.A., 1991. Factors governing cathodoluminescence in calcite and dolomite, and their implications for studies of  
1166 carbonate diagenesis.
- 1167 Malumian, N., Nanez, C., 2011. The Late Cretaceous–Cenozoic transgressions in Patagonia and the Fuegian Andes: foraminifera,  
1168 palaeoecology, and palaeogeography. *Biological Journal of the Linnean Society* 103, 269–288.
- 1169 McConnaughey, T., 1989.  $^{13}\text{C}$  and  $^{18}\text{O}$  isotopic disequilibrium in biological carbonates: II. In vitro simulation of kinetic isotope effects.  
1170 *Geochimica et Cosmochimica Acta* 53, 163–171.
- 1171 McConnaughey, T.A., Burdett, J., Whelan, J.F., Paull, C.K., 1997. Carbon isotopes in biological carbonates: Respiration and photosynthesis.  
1172 *Geochimica et Cosmochimica Acta* 61, 611–622. doi:10.1016/S0016-7037(96)00361-4
- 1173 McConnaughey, T.A., Gillikin, D.P., 2008. Carbon isotopes in mollusk shell carbonates. *Geo-Marine Letters* 28, 287–299.
- 1174 Miller, K.G., Sugarman, P.J., Browning, J.V., Kominz, M.A., Hernández, J.C., Olsson, R.K., Wright, J.D., Feigenson, M.D., Van Sickle,  
1175 W., 2003. Late Cretaceous chronology of large, rapid sea-level changes: Glacioeustasy during the greenhouse world. *Geology*  
1176 31, 585–588.
- 1177 Morrison, J.M., Codispoti, L.A., Gaurin, S., Jones, B., Manghni, V., Zheng, Z., 1998. Seasonal variation of hydrographic and nutrient  
1178 fields during the US JGOFS Arabian Sea Process Study. *Deep Sea Research Part II: Topical Studies in Oceanography* 45, 2053–  
1179 2101.
- 1180 Mouchi, V., De Rafélis, M., Lartaud, F., Fialin, M., Verrecchia, E., 2013. Chemical labelling of oyster shells used for time-calibrated high-  
1181 resolution Mg/Ca ratios: a tool for estimation of past seasonal temperature variations. *Palaeogeography, Palaeoclimatology,*  
1182 *Palaeoecology* 373, 66–74.
- 1183 Müller, A.H., 1970. Zur funktionellen Morphologie, Taxilogie und Ökologie von Pycnodonta (*Ostreina*, Lamellibranchiata).  
1184 *Monatsberichte der Deutschen Akademie der Wissenschaften zu Berlin* 12, 902–923.
- 1185 Nestler, H., 1965. Entwicklung und Schalenstruktur von Pycnodonte uesticularis (LAM.) und Dimyodon nilssoni (v. Hag.) aus der  
1186 Oberkreide. *Geologie* 14, 64–77.
- 1187 O'Brien, C.L., Robinson, S.A., Pancost, R.D., Sinnighe Damsté, J.S., Schouten, S., Lunt, D.J., Alsenz, H., Bornemann, A., Bottini, C.,  
1188 Brassell, S.C., Farnsworth, A., Forster, A., Huber, B.T., Inglis, G.N., Jenkyns, H.C., Linnert, C., Littler, K., Markwick, P.,  
1189 McAnena, A., Mutterlose, J., Naafs, B.D.A., Püttmann, W., Sluijs, A., van Helmond, N.A.G.M., Vellekoop, J., Wagner, T.,  
1190 Wrobel, N.E., 2017. Cretaceous sea-surface temperature evolution: Constraints from TEX 86 and planktonic foraminiferal  
1191 oxygen isotopes. *Earth-Science Reviews* 172, 224–247. doi:10.1016/j.earscirev.2017.07.012
- 1192 Omata, T., Suzuki, A., Kawahat, H., Okamoto, M., 2005. Annual fluctuation in the stable carbon isotope ratio of coral skeletons: the relative  
1193 intensities of kinetic and metabolic isotope effects. *Geochimica et cosmochimica acta* 69, 3007–3016.
- 1194 Otto-Bliessner, B.L., Brady, E.C., Shields, C., 2002. Late Cretaceous ocean: Coupled simulations with the National Center for Atmospheric  
1195 Research Climate System Model. *J. Geophys. Res.* 107, ACL 11-1. doi:10.1029/2001JD000821
- 1196 Owen, R., Kennedy, H., Richardson, C., 2002. Experimental investigation into partitioning of stable isotopes between scallop (*Pecten*  
1197 *maximus*) shell calcite and sea water. *Palaeogeography, Palaeoclimatology, Palaeoecology* 185, 163–174.
- 1198 Palazzesi, L., Barreda, V., 2007. Major vegetation trends in the Tertiary of Patagonia (Argentina): a qualitative paleoclimatic approach  
1199 based on palynological evidence. *Flora-Morphology, Distribution, Functional Ecology of Plants* 202, 328–337.
- 1200 Pearson, P.N., Ditchfield, P.W., Singano, J., Harcourt-Brown, K.G., Nicholas, C.J., Olsson, R.K., Shackleton, N.J., Hall, M.A., 2001. Warm  
1201 tropical sea surface temperatures in the Late Cretaceous and Eocene epochs. *Nature* 413, 481–487.
- 1202 Pennington, J.T., Chavez, F.P., 2000. Seasonal fluctuations of temperature, salinity, nitrate, chlorophyll and primary production at station  
1203 H3/M1 over 1989–1996 in Monterey Bay, California. *Deep Sea Research Part II: Topical Studies in Oceanography* 47, 947–973.
- 1204 Petersen, S.V., Winkelstern, I.Z., Lohmann, K.C., Meyer, K.W., 2016. The effects of Porapak™ trap temperature on  $\delta^{18}\text{O}$ ,  $\delta^{13}\text{C}$ , and  $\Delta 47$   
1205 values in preparing samples for clumped isotope analysis. *Rapid Communications in Mass Spectrometry* 30, 199–208.
- 1206 Pirrie, D., Marshall, J.D., 1990. Diagenesis of *Inoceramus* and Late Cretaceous paleoenvironmental geochemistry: a case study from James  
1207 Ross Island, Antarctica. *Palaios* 336–345.
- 1208 Pramparo, M.B., Papu, O.H., 2006. Late Maastrichtian dinoflagellate cysts from the Cerro Butaló section, southern Mendoza province,  
1209 Argentina. *Journal of Micropalaeontology* 25, 23–33.
- 1210 Prámparo, M.B., Papu, O.H., Milana, J.P., 1996. Estudios palinológicos del miembro inferior de la Formación Pachaco, Terciano de la  
1211 provincia de San Juan. *Descripciones sistemáticas. Ameghiniana* 33, 397–407.
- 1212 Pugaczewska, H., 1977. The Upper Cretaceous *Ostreidae* from the Middle Vistula Region (Poland). *Acta palaeontologica polonica* 22.  
1213 Quan, C., Sun, C., Sun, Y., Sun, G., 2009. High resolution estimates of paleo- $\text{CO}_2$  levels through the Campanian (Late Cretaceous) based  
1214 on Ginkgo cuticles. *Cretaceous Research* 30, 424–428.
- 1215 Ravelo, A.C., Hillaire-Marcel, C., 2007. Chapter Eighteen the use of oxygen and carbon isotopes of foraminifera in Paleooceanography.  
1216 *Developments in Marine Geology* 1, 735–764.
- 1217 Richardson, C.A., Peharda, M., Kennedy, H., Kennedy, P., Onofri, V., 2004. Age, growth rate and season of recruitment of *Pinna nobilis* (L)  
1218 in the Croatian Adriatic determined from Mg: Ca and Sr: Ca shell profiles. *Journal of Experimental Marine Biology and Ecology*  
1219 299, 1–16.
- 1220 Romanek, C.S., Grossman, E.L., Morse, J.W., 1992. Carbon isotopic fractionation in synthetic aragonite and calcite: effects of temperature  
1221 and precipitation rate. *Geochimica et Cosmochimica Acta* 56, 419–430.
- 1222 Rosenberg, G.D., Hughes, W.W., 1991. A metabolic model for the determination of shell composition in the bivalve mollusc, *Mytilus*  
1223 *edulis*. *Lethaia* 24, 83–96.
- 1224 Scasso, R.A., Concheyro, A., Kiessling, W., Aberhan, M., Hecht, L., Medina, F.A., Tagle, R., 2005. A tsunami deposit at the  
1225 Cretaceous/Paleogene boundary in the Neuquén Basin of Argentina. *Cretaceous Research* 26, 283–297.
- 1226 Schlager, W., James, N.P., 1978. Low-magnesian calcite limestones forming at the deep-sea floor, Tongue of the Ocean, Bahamas.  
1227 *Sedimentology* 25, 675–702.
- 1228 Schouten, S., Hopmans, E. C., & Damsté, J. S. S. 2013. The organic geochemistry of glycerol dialkyl glycerol tetraether lipids: a  
1229 review. *Organic geochemistry*, 54, 19–61.
- 1230 Schöne, B.R., Fiebig, J., Pfeiffer, M., Gleß, R., Hickson, J., Johnson, A.L., Dreyer, W., Oschmann, W., 2005a. Climate records from a  
1231 bivalve *Methuselah* (*Arctica islandica*, Mollusca; Iceland). *Palaeogeography, Palaeoclimatology, Palaeoecology* 228, 130–148.



- 1232 Schöne, B.R., Houk, S.D., Castro, A.D.F., Fiebig, J., Oschmann, W., Kröncke, I., Dreyer, W., Gosselck, F., 2005b. Daily growth rates in  
 1233 shells of Arctic Icelandica: assessing sub-seasonal environmental controls on a long-lived bivalve mollusk. *Palaios* 20, 78–92.  
 1234 Servicio Meteorológico Nacional, Republic of Argentina,  
 1235 <http://www.smn.gov.ar/serviciosclimaticos/?mod=turismo&id=5&var=buenosaires>, visited on 25-09-2017.  
 1236 Stanley, S.M., Hardie, L.A., 1998. Secular oscillations in the carbonate mineralogy of reef-building and sediment-producing organisms  
 1237 driven by tectonically forced shifts in seawater chemistry. *Palaeogeography, Palaeoclimatology, Palaeoecology* 144, 3–19.  
 1238 Stenzel, H. B. 1956. Cretaceous oysters of southwestern North America. *Int. Geol. Congr. Mexico City*, 15-37.  
 1239 Stenzel, H.B., 1971. Oysters. University of Kansas Press and Geological Society of America, Part N, Mollusca.  
 1240 Steuber, T., 1999. Isotopic and chemical intra-shell variations in low-Mg calcite of rudist bivalves (Mollusca-Hippuritacea): disequilibrium  
 1241 fractionations and late Cretaceous seasonality. *International Journal of Earth Sciences* 88, 551–570.  
 1242 Steuber, T., 1996. Stable isotope sclerochronology of rudist bivalves: Growth rates and Late Cretaceous seasonality. *Geology* 24, 315.  
 1243 doi:10.1130/0091-7613(1996)024<0315:SISORB>2.3.CO;2  
 1244 Steuber, T., Rauch, M., Masse, J.-P., Graaf, J., Malkoč, M., 2005. Low-latitude seasonality of Cretaceous temperatures in warm and cold  
 1245 episodes. *Nature* 437, 1341–1344.  
 1246 Surge, D., Lohmann, K.C., 2008. Evaluating Mg/Ca ratios as a temperature proxy in the estuarine oyster, *Crassostrea virginica*. *J. Geophys.*  
 1247 *Res.* 113, G02001. doi:10.1029/2007JG000623  
 1248 Surge, D., Lohmann, K.C., Dettman, D.L., 2001. Controls on isotopic chemistry of the American oyster, *Crassostrea virginica*: implications  
 1249 for growth patterns. *Palaeogeography, Palaeoclimatology, Palaeoecology* 172, 283–296.  
 1250 Surge, D., Owens, S., 2003. Oxygen and Carbon Stable Isotope and Sr: Ca Records in Outer and Middle Microstructural Layers of Bivalve  
 1251 Shells (*Mercenaria campechiensis*). in: AGU Fall Meeting Abstracts.  
 1252 Takesue, R.K., van Geen, A., 2004. Mg/Ca, Sr/Ca, and stable isotopes in modern and Holocene *Protothaca staminea* shells from a northern  
 1253 California coastal upwelling region. *Geochimica et Cosmochimica Acta* 68, 3845–3861.  
 1254 Titschack, J., Zuschin, M., Spötl, C., Baal, C., 2010. The giant oyster *Hytotissa hyotis* from the northern Red Sea as a decadal-scale archive  
 1255 for seasonal environmental fluctuations in coral reef habitats. *Coral Reefs* 29, 1061–1075.  
 1256 Torsvik, T.H., Van der Voo, R., Preeden, U., Mac Niocail, C., Steinberger, B., Doubrovine, P.V., van Hinsbergen, D.J., Domeier, M.,  
 1257 Gaina, C., Tohver, E., others, 2012. Phanerozoic polar wander, palaeogeography and dynamics. *Earth-Science Reviews* 114,  
 1258 325–368.  
 1259 Tripathi, A., Zachos, J., Marincovich Jr., L., Bice, K., 2001. Late Paleocene Arctic coastal climate inferred from molluscan stable and  
 1260 radiogenic isotope ratios. *Palaeogeography, Palaeoclimatology, Palaeoecology* 170, 101–113. doi:10.1016/S0031-  
 1261 0182(01)00230-9  
 1262 Ullmann, C.V., Böhm, F., Rickaby, R.E., Wiechert, U., Korte, C., 2013. The Giant Pacific Oyster (*Crassostrea gigas*) as a modern analog for  
 1263 fossil ostreoids: isotopic (Ca, O, C) and elemental (Mg/Ca, Sr/Ca, Mn/Ca) proxies. *Geochemistry, Geophysics, Geosystems* 14,  
 1264 4109–4120.  
 1265 Ullmann, C.V., Wiechert, U., Korte, C., 2010. Oxygen isotope fluctuations in a modern North Sea oyster (*Crassostrea gigas*) compared with  
 1266 annual variations in seawater temperature: Implications for palaeoclimate studies. *Chemical Geology* 277, 160–166.  
 1267 doi:10.1016/j.chemgeo.2010.07.019  
 1268 van Hinsbergen, D.J., de Groot, L.V., van Schaik, S.J., Spakman, W., Bijl, P.K., Sluijs, A., Langereis, C.G., Brinkhuis, H., 2015a. A  
 1269 paleolatitude calculator for paleoclimate studies. *PLoS one* 10, e0126946.  
 1270 van Hinsbergen, D.J., de Groot, L.V., van Schaik, S.J., Spakman, W., Bijl, P.K., Sluijs, A., Langereis, C.G., Brinkhuis, H., 2015b. A  
 1271 paleolatitude calculator for paleoclimate studies. *PLoS one* 10, e0126946.  
 1272 Van Rimpelbergh, M., Verheyden, S., Allan, M., Quinif, Y., Keppens, E., Claeys, P., 2014. Seasonal variations recorded in cave monitoring  
 1273 results and a 10 year monthly resolved speleothem  $\delta^{18}\text{O}$  and  $\delta^{13}\text{C}$  record from the Han-sur-Lesse cave, Belgium. *Climate of the*  
 1274 *Past Discussions* 10, 1821–1856.  
 1275 Vander Putten, E., Dehairs, F., Keppens, E., Baeyens, W., 2000. High resolution distribution of trace elements in the calcite shell layer of  
 1276 modern *Mytilus edulis*: Environmental and biological controls. *Geochimica et Cosmochimica Acta* 64, 997–1011.  
 1277 Vansteeneberge, S., Verheyden, S., Goderis, S., Sinnesael, M., de Winter, N.J., Van Malderen, S.J.M., Vanhaecke, F., Claeys, P.,  
 1278 Reconstructing seasonality through stable isotope and trace element analysis of the Proserpine stalagmite, Han-sur-Lesse Cave,  
 1279 Belgium: indications for climate-driven changes during the last 400 years. *Chemical Geology*, in review.  
 1280 Veizer, J., 1983. Chemical diagenesis of carbonates: theory and application of trace element technique.  
 1281 Vellekoop, J., Esmerary-Senlet, S., Miller, K.G., Browning, J.V., Sluijs, A., van de Schootbrugge, B., Damsté, J.S.S., Brinkhuis, H., 2016.  
 1282 Evidence for Cretaceous-Paleogene boundary bolide “impact winter” conditions from New Jersey, USA. *Geology* 44, 619–622.  
 1283 Vermeij, G.J., 2014. The oyster enigma variations: a hypothesis of microbial calcification. *Paleobiology* 40, 1–13.  
 1284 Videt, B. 2004. Dynamique des paléoenvironnements à huîtres du Crétacé supérieur nord-aquitain (SW France) et du Mio-Pliocène  
 1285 andalou (SE Espagne): biodiversité, analyse séquentielle, biogéochimie. – *Mém. Géosc. Rennes*, 108, 1-261  
 1286 Wanamaker Jr, A.D., Kreutz, K.J., Wilson, T., Borns Jr, H.W., Introne, D.S., Feindel, S., 2008. Experimentally determined Mg/Ca and  
 1287 Sr/Ca ratios in juvenile bivalve calcite for *Mytilus edulis*: implications for paleotemperature reconstructions. *Geo-Marine Letters*  
 1288 28, 359–368.  
 1289 Wang, W.-X., Fisher, N.S., 1996. Assimilation of trace elements and carbon by the mussel *Mytilus edulis*: effects of food composition.  
 1290 *Limnology and Oceanography* 4, 1.  
 1291 Wang, Q.J., Xu, X.H., Jin, P.H., Li, R.Y., Li, X.Q., Sun, B.N., 2013. Quantitative reconstruction of Mesozoic paleoatmospheric CO<sub>2</sub> based  
 1292 on stomatal parameters of fossil *Baiera furcata* of Ginkgophytes. *Geological review* 59, 1035–1045.  
 1293 Watanabe, T., Winter, A., Oba, T., 2001. Seasonal changes in sea surface temperature and salinity during the Little Ice Age in the Caribbean  
 1294 Sea deduced from Mg/Ca and 18 O/16 O ratios in corals. *Marine Geology* 173, 21–35.  
 1295 Weidman, C.R., Jones, G.A., 1994. The long-lived mollusc *Arctica islandica*: A new paleoceanographic tool for the reconstruction of  
 1296 bottom temperatures for the continental shelves of the northern North Atlantic Ocean. *Journal of Geophysical Research: Oceans*  
 1297 99, 18305–18314.  
 1298 Weiner, S., Dove, P.M., 2003. An overview of biomineralization processes and the problem of the vital effect. *Reviews in mineralogy and*  
 1299 *geochemistry* 54, 1–29.  
 1300 Wisshak, M., Correa, M.L., Gofas, S., Salas, C., Taviani, M., Jakobsen, J., Freiwald, A., 2009. Shell architecture, element composition, and  
 1301 stable isotope signature of the giant deep-sea oyster *Neopycnodonte zibrowii* sp. n. from the NE Atlantic. *Deep Sea Research*  
 1302 *Part I: Oceanographic Research Papers* 56, 374–407.  
 1303 Woelders, L., Vellekoop, J., Kroon, D., Smit, J., Casado, S., Prámparo, M.B., Dinarès-Turell, J., Peterse, F., Sluijs, A., Lenaerts, J.T.M.,  
 1304 Speijer, R.P., 2017. Latest Cretaceous climatic and environmental change in the South Atlantic region. *Paleoceanography*  
 1305 2016PA003007. doi:10.1002/2016PA003007  
 1306 Woo, K.-S., Anderson, T.F., Sandberg, P.A., 1993. Diagenesis of skeletal and nonskeletal components of mid-Cretaceous limestones.

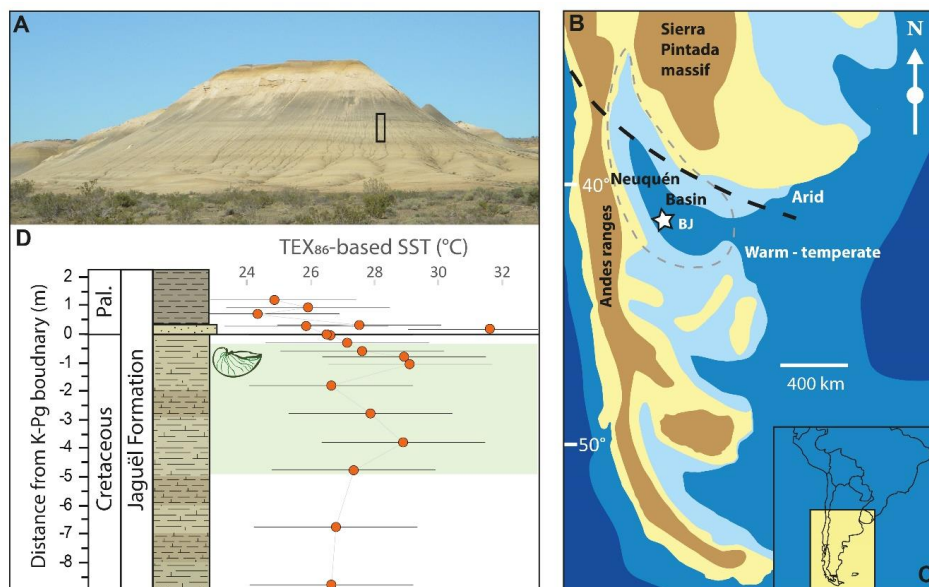


1307 Journal of Sedimentary Research 63.

1308

1309

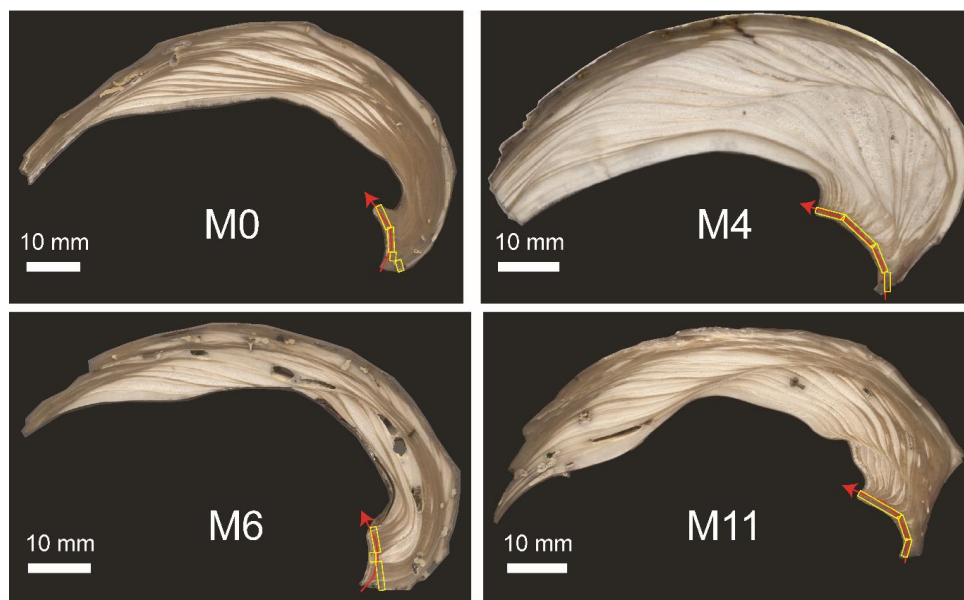
1310 [FIGURE CAPTIONS]



1311

1312 **Figure 1**

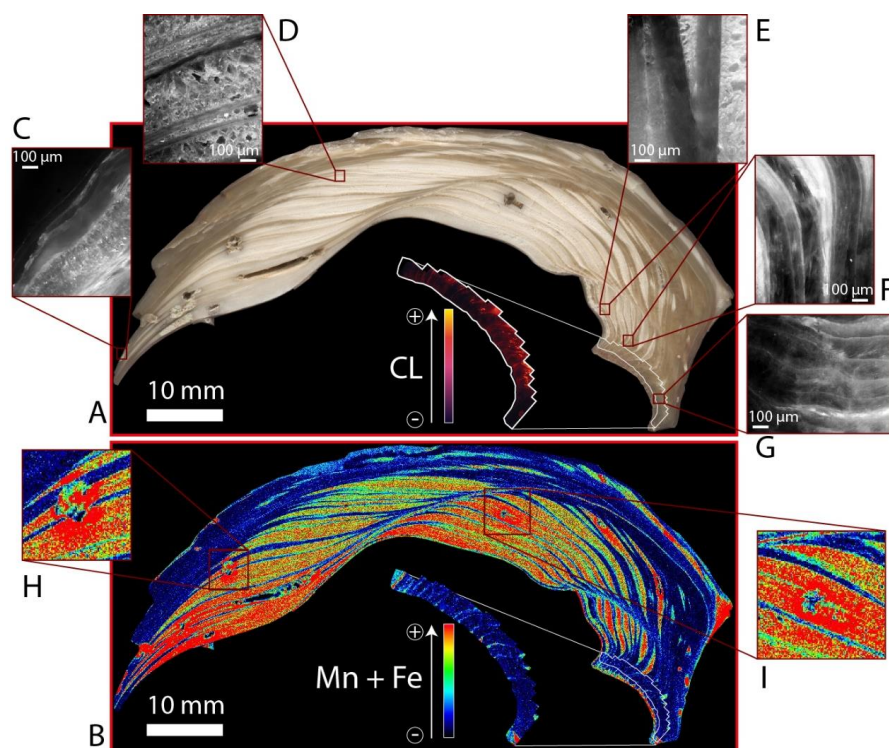
1313 Origin and stratigraphy of the studied *Pycnodonte vesicularis* specimens. A) photograph of the  
1314 Bajada de Jaguël section (BJ; modern location: 38°06'10.5"S, 68°23'20.5"W, palaeolatitude =  
1315 43°S). B) Palaeogeography of study area during the latest Cretaceous. Palaeomap after  
1316 Scasso et al. (2005) and Woelders et al. (2017). C) Location of the study area in southern  
1317 Argentina relative to modern day South America. D) lithology, stratigraphy and TEX<sub>86</sub> record  
1318 (Woelders et al., 2017) of the BJ section. The main *P. vesicularis* level is indicated in light  
1319 green.



1320  
1321  
1322  
1323  
1324  
1325

**Figure 2**

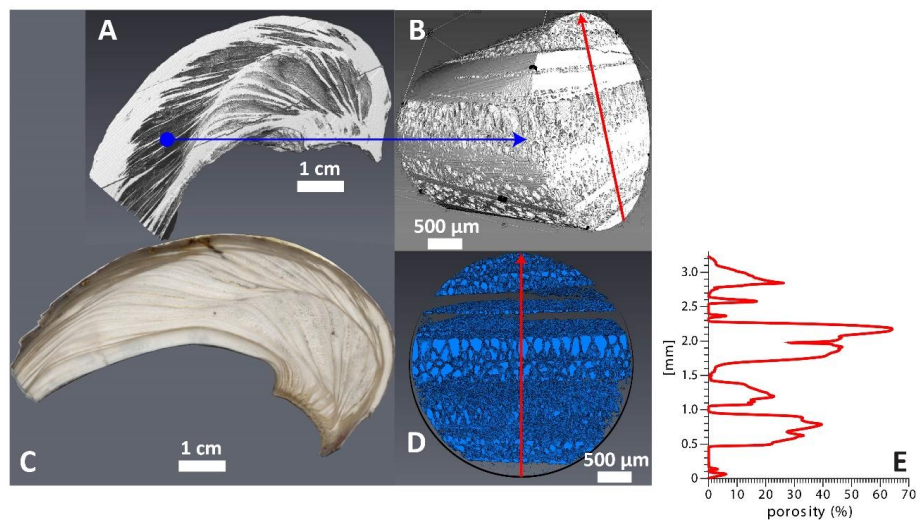
Colour scans of cross sections of the four shells subject to multi-proxy analysis. Red arrows indicate sampling location and direction. Yellow boxes indicate the location of stable isotope transects.



1326  
1327  
1328  
1329  
1330  
1331  
1332  
1333  
1334  
1335  
1336  
1337  
1338  
1339  
1340

**Figure 3**

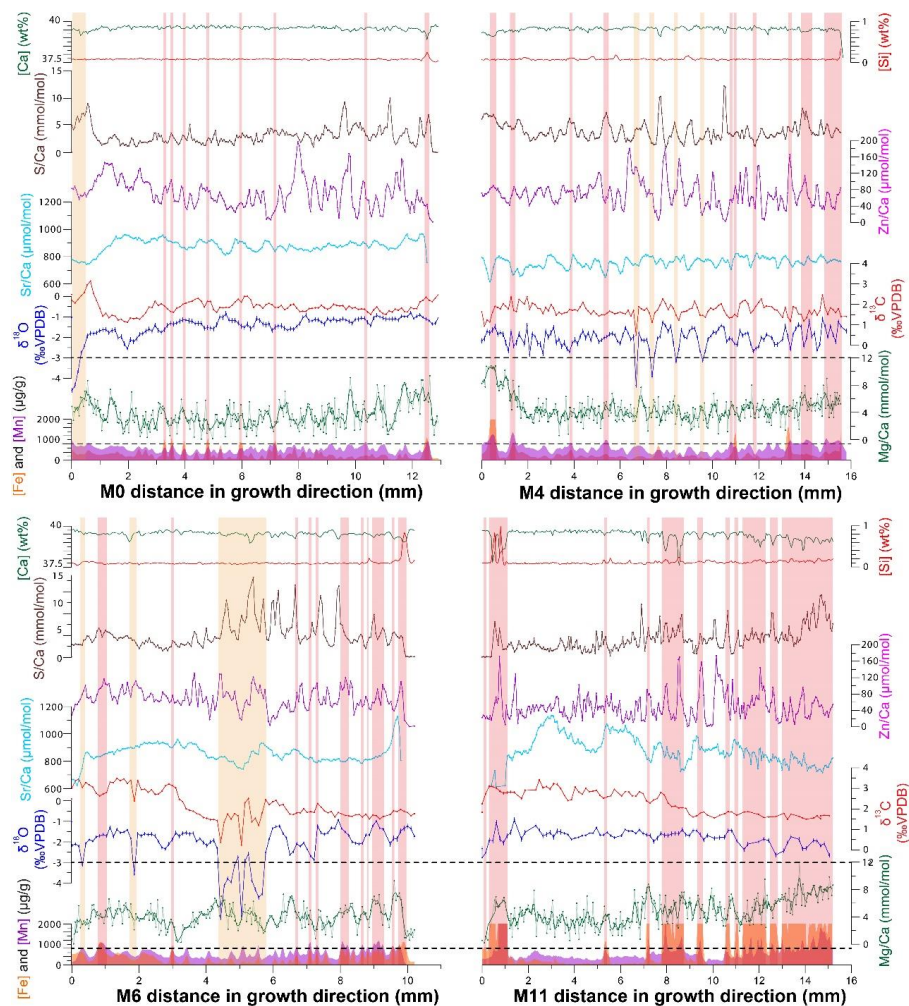
Overview of the results of colour scanning, microscopic analyses and  $\mu$ XRF mapping of specimen M11. A) Colour scan of cross section in growth direction through the shell, with close-up of cathodoluminescence microscopic image of the hinge line. B)  $\mu$ XRF mapping of the cross section, with close-up of the  $\mu$ XRF map of the hinge line. C) Optical microscopic image of transitions between dense foliated calcite and porous vesicular calcite. Note the blocky calcite crystals in the vesicular structure. D) Optical microscopic image of very thin, alternating layers of foliated and vesicular calcite. E) Optical microscopic image of sharp transitions between dense foliated calcite and porous vesicular calcite F) Optical microscopic image of more gradual transitions between foliated calcite and vesicular calcite. G) Optical microscopic image of dense, foliated calcite layers in shell hinge line. Note the thin layer of vesicular calcite (white) intercalated between the foliated layers near the bottom of the image. H) and I) Close-up of  $\mu$ XRF mapping of bore hole with corona of elevated Fe and Mn concentrations.



1341  
1342  
1343  
1344  
1345  
1346  
1347  
1348  
1349  
1350

**Figure 4**

Overview of the results of CT-scanning and pore analysis on specimen M4, with A) showing an overview of density variations in the shell (white = dense calcite, darker colours represent porosity). The blue dot shows the location of the part of the shell that was CT-scanned at high resolution. B) shows the shape and density of a part of the shell that was CT-scanned with higher spatial resolution as well as the location of the porograph shown in E). C) shows a colour scan of the shell cross section. D) shows a cross-section through the high-resolution section through the shell with porosity in blue. E) shows a graph of porosity through the high resolution section perpendicular to the growth layers.

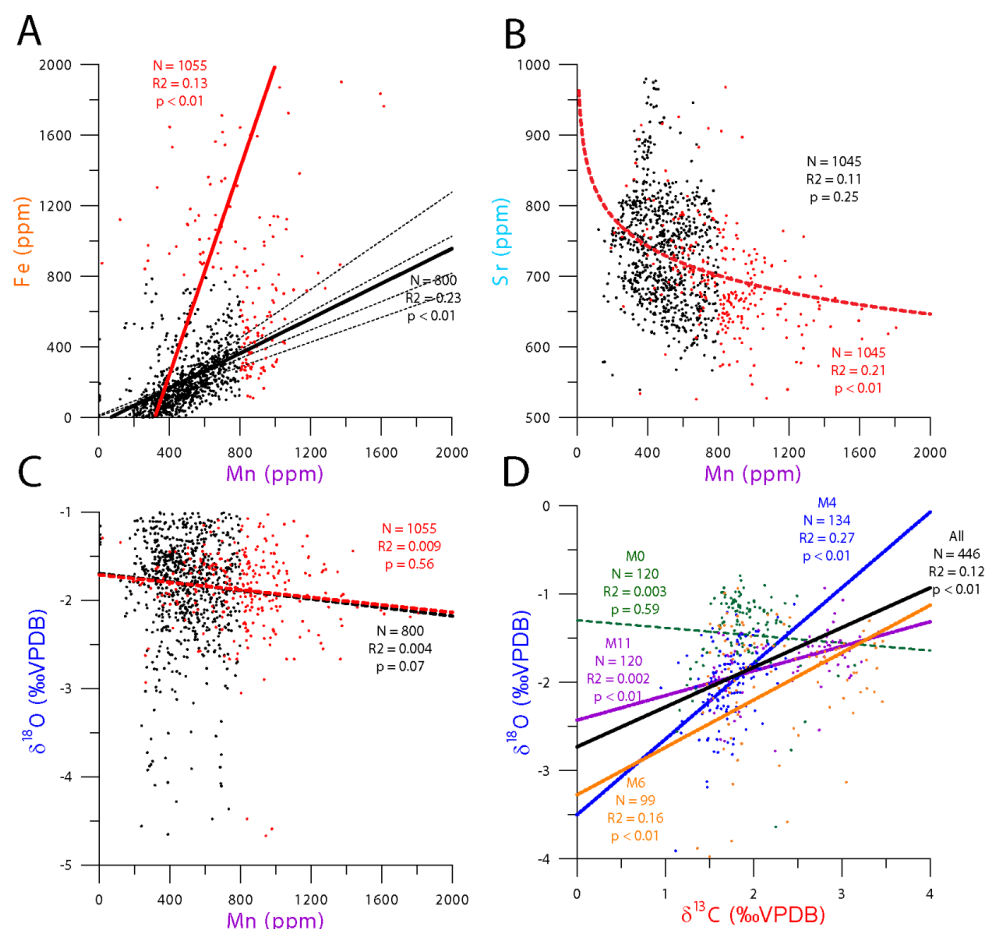


1351

1352

**Figure 5**

1353 Overview of multi-proxy records through the hinges of 4 specimens of *P. vesicularis*. From top to  
1354 bottom, records of [Ca] (green), [Si] (red), S/Ca ratios (brown), Zn/Ca ratios (purple), Sr/Ca  
1355 ratios (light blue),  $\delta^{13}\text{C}$  (red),  $\delta^{18}\text{O}$  (blue), Mg/Ca (green), [Mn] (purple) and [Fe] (orange) are  
1356 shown. Red arrows in Figure 2 indicate the direction of sampling. Vertical bars indicate parts  
1357 of the records that were affected by diagenesis based on Mn and Fe concentrations (red bars) and stable isotope ratios (orange bars). Note that the vertical scale of the Mn and Fe  
1358 plots is clipped at 2000  $\mu\text{g/g}$ .  
1359

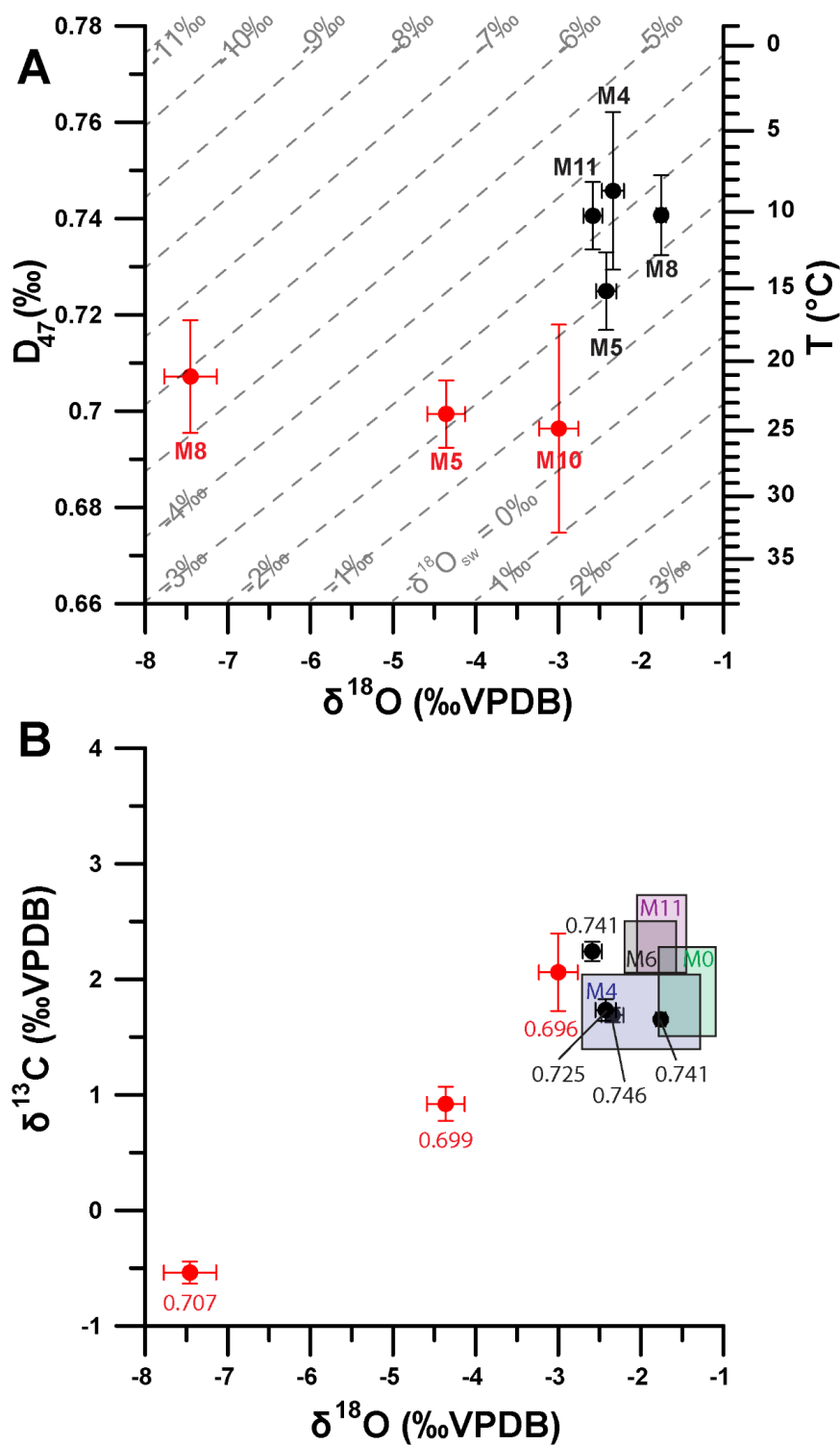


1360  
 1361  
 1362  
 1363  
 1364  
 1365  
 1366  
 1367  
 1368  
 1369  
 1370  
 1371  
 1372

**Figure 6**

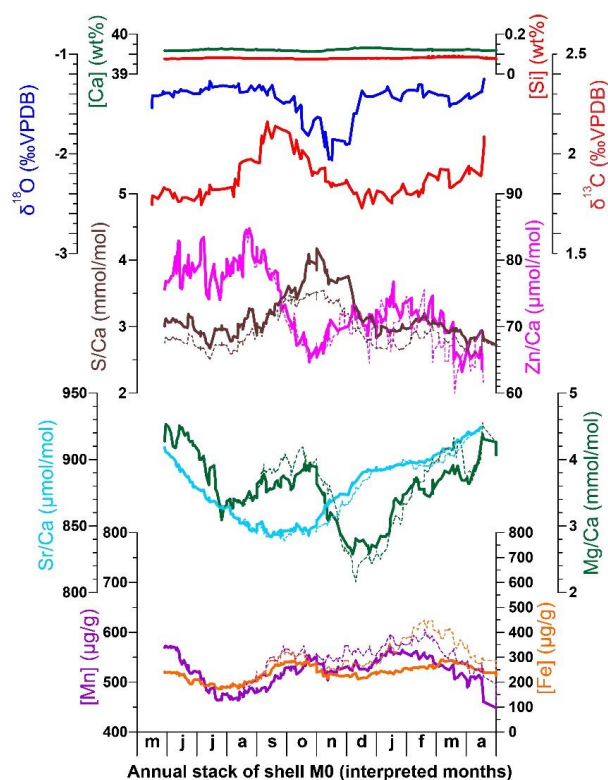
Cross plots showing cross plots between trace element and stable isotope measurements in the shells. Black lines indicate correlations through all measurements, red lines show correlations of diagenetically altered samples (according to the 800 µg/g threshold for Fe and Mn) and alternatively coloured lines indicate correlations in individual shells. Statistics of the regressions are indicated in matching colours. A) [Fe] vs [Mn] showing how both elements increase with increasing diagenetic overprinting. Steeper slopes suggest relatively more Fe is added in diagenetically altered samples. B) [Sr] vs [Mn] showing decreasing Sr concentrations corresponding to increasing [Mn], but only in diagenetically altered samples. C) δ<sup>18</sup>O vs [Mn] showing lack of correlation, although Mn-rich diagenetic samples generally have lower δ<sup>18</sup>O values. D) δ<sup>18</sup>O vs δ<sup>13</sup>C, showing positive correlation in specimens affected by diagenesis and no correlation in M0, which has pristine values.



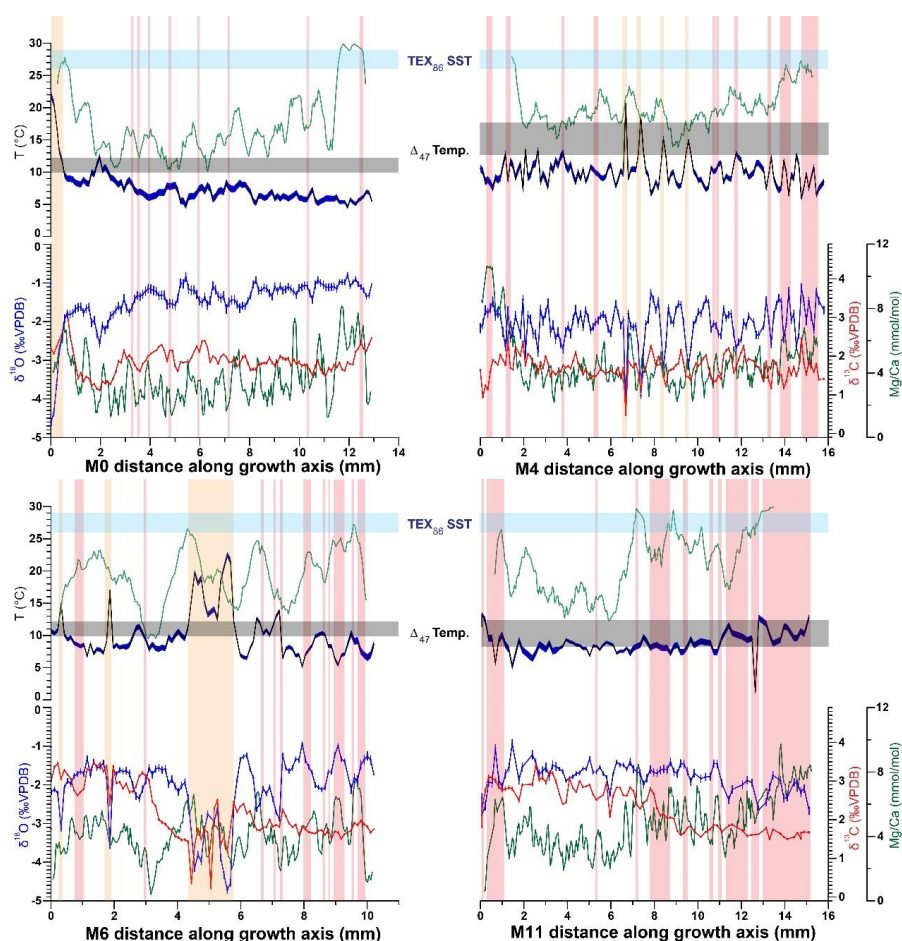




1374 **Figure 7**  
 1375 Cross plots of clumped isotope results. A)  $\Delta_{47}$  vs.  $\delta^{18}\text{O}$  from clumped isotope measurements on all  
 1376 seven shells. Red dots and error bars represent measurements of samples from the ventral  
 1377 margin of the shells, while black dots and error bars indicate results from dense foliated  
 1378 calcite from the hinge of the shells. Dashed lines illustrate the  $\delta^{18}\text{O}$  values of seawater that  
 1379 correspond to the combination of  $\Delta_{47}$  and  $\delta^{18}\text{O}$  values in the graph. B)  $\delta^{13}\text{C}$  vs.  $\delta^{18}\text{O}$  from  
 1380 clumped isotope measurements on all shells. Red dots and error bars represent  
 1381 measurements of samples from the ventral margin of the shells, while black dots and error bars  
 1382 indicate results from dense foliated calcite from the hinge of the shells. Numbers next  
 1383 to the dots indicate  $\Delta_{47}$  values measured in the same samples. Coloured rectangles indicate  
 1384 the range of pristine stable isotope values measured in high resolution transects through the  
 1385 hinges of shells M0, M4, M6 and M11.  
 1386



1387 **Figure 8**  
 1388 Stack of proxy records shell M0 made according to a tentative interpretation of annual cyclicly  
 1389 based on Sr/Ca ratios in **Figure 5**. Solid lines indicate annual stacks excluding diagenetically  
 1390 altered samples while dashed lines include all measured samples to show the effect of  
 1391 diagenesis. From top to bottom, stacks of [Ca] (green), [Si] (red),  $\delta^{13}\text{C}$  (red),  $\delta^{18}\text{O}$  (blue), S/Ca  
 1392 ratios (brown), Zn/Ca ratios (purple), Sr/Ca ratios (light blue), Mg/Ca (green), [Mn] (purple)  
 1393 and [Fe] (orange) records are shown. Subdivisions of the stack into 12 time steps and  
 1394 corresponding months are based on an interpretation of the phase relationship between the  
 1395 proxies in terms of palaeoenvironmental seasonality.  
 1396



1397  
 1398  
 1399  
 1400  
 1401  
 1402  
 1403  
 1404  
 1405  
 1406  
 1407  
 1408  
 1409  
 1410  
 1411

**Figure 9**

Overview of stable isotope and Mg/Ca records (bottom) as well as tentative temperature and salinity reconstructions (top) based on  $\delta^{18}\text{O}$  (blue) and Mg/Ca (green), clumped isotope analysis (grey bars) and  $\text{TEX}_{86}^{\text{H}}$  palaeothermometry (light blue bars). Temperatures calculated from  $\delta^{18}\text{O}$  records (dark blue on top) are based on the calibration by Kim and O'Neil (1997) and the  $\delta^{18}\text{O}_{\text{sw}}$  value of the clumped isotope measurements indicated in grey. Mg/Ca temperatures (green line on top) were calculated using the calibration reported in Surge and Lohmann (2008) with a factor 3.3 correction for lower Mg/Ca ratios in late Cretaceous ocean water. Temperatures of bulk samples of shells M4 and M11 measured using clumped isotope analysis are indicated by grey bars in graphs of M0 and M6 represent average clumped isotope temperatures of all pristine shell samples (see **Table 1**). Red and orange vertical bars indicate intervals where vesicular calcite was incorporated in the stable isotopic measurements (see **Figure 5**).



Shell name	Sampling Location	N	$\delta^{13}\text{C}_{\text{Cav}}$ (VPDB) $\pm 1\sigma$	$\delta^{13}\text{C}_{\text{record}}$ (VPDB) $\pm \text{season}$	$\delta^{18}\text{O}_{\text{av}}$ (VPDB) $\pm 1\sigma$	$\delta^{18}\text{O}_{\text{record}}$ (VPDB) $\pm \text{season}$	$\Delta_{47}$ $\pm 1\sigma$	$T_{\text{av}}$ (°C) $\pm 1\sigma$	$\delta^{18}\text{O}_{\text{sw}}$ $\pm 1\sigma$
M0	Shell hinge			1.91 $\pm$ 0.38		-1.43 $\pm$ 0.35			
M4	Shell hinge	3	1.74 $\pm$ 0.10	1.73 $\pm$ 0.32	-2.42 $\pm$ 0.12	-1.99 $\pm$ 0.72	0.725 $\pm$ 0.008	15.2 $\pm$ 2.6	-2.1 $\pm$ 0.7
M5	Shell hinge	3	1.70 $\pm$ 0.06		-2.34 $\pm$ 0.13		0.746 $\pm$ 0.016	9.0 $\pm$ 4.9	-3.4 $\pm$ 1.2
M6	Shell hinge			2.28 $\pm$ 0.23		-1.88 $\pm$ 0.31			
M8	Shell hinge	4	1.66 $\pm$ 0.02		-1.75 $\pm$ 0.06		0.741 $\pm$ 0.008	10.3 $\pm$ 2.5	-2.5 $\pm$ 0.6
M11	Shell hinge	4	2.25 $\pm$ 0.08	2.40 $\pm$ 0.34	-2.58 $\pm$ 0.11	-1.74 $\pm$ 0.30	0.741 $\pm$ 0.007	10.3 $\pm$ 2.1	-3.3 $\pm$ 0.6
M5	Ventral margin	4	0.93 $\pm$ 0.15		-4.36 $\pm$ 0.23		0.699 $\pm$ 0.007	23.8 $\pm$ 2.5	-2.2 $\pm$ 0.7
M8	Ventral margin	4	-0.53 $\pm$ 0.10		-7.45 $\pm$ 0.32		0.707 $\pm$ 0.012	21.3 $\pm$ 4.0	-5.9 $\pm$ 1.1
M10	Ventral margin	3	2.07 $\pm$ 0.34		-2.99 $\pm$ 0.23		0.696 $\pm$ 0.022	25.4 $\pm$ 7.7	-0.6 $\pm$ 1.8
Average	Shell hinge	14					0.738 $\pm$ 0.004	11.1 $\pm$ 1.2	-2.8 $\pm$ 0.6
Average	Ventral margin	11					0.643 $\pm$ 0.007	23.3 $\pm$ 2.9	-3.1 $\pm$ 2.5

1412

1413

**Table 1**

1414

Overview table of stable and clumped isotope results in this study. Rows highlighted in red represent samples from the ventral margin of the shells (which contain vesicular calcite). Rows with a white background represent samples of the dense foliated shell hinge. Note that for some shells (M5 and M8) both the ventral margin and the shell hinge was measured. Columns labelled “ $\delta^{13}\text{C}_{\text{record}}$ ” and “ $\delta^{18}\text{O}_{\text{record}}$ ” contain averages of the high-resolution stable isotope records measured in the shell hinges (if available, Figure 5). The bottom two rows contain average  $\Delta_{47}$  and  $\delta^{18}\text{O}_{\text{sw}}$  values of shell hinge (white) and ventral margin (red) samples, highlighting the difference between the two sampling strategies.

1415

1416

1417

1418

1419

1420

1421